Journal of
Microscopy

Journal of Microscopy, Vol. 259, Issue 3 2015, pp. 237–256 doi: 10.1111/jmi.12258
Received 30 October 2014; accepted 25 March 2015

Making EBSD on water ice routine

D.J. PRIOR*, K. LILLY*, M. SEIDEMANN*, M. VAUGHAN*, L. BECROFT*, R. EASINGWOOD†, S. DIEBOLD‡, R. OBBARD§, C. DAGHLIAN§, I. BAKER§, T. CASWELL‖, N. GOLDING#, D. GOLDSBY**, W.B. DURHAM#, S. PIAZOLO†† & C.J.L. WILSON‡‡

*Department of Geology, University of Otago, Dunedin, New Zealand

†Otago Centre for Electron Microscopy, University of Otago, Dunedin, New Zealand

‡Universiteit Utrecht, Department of Earth Sciences, Utrecht, Netherlands

§Thayer School of Engineering, Dartmouth College, Hanover, New Hampshire, U.S.A.

‖Department of Earth, Environmental and Planetary Studies, Brown University, Providence, Rhode Island, U.S.A.

#Earth Atmosphere and Planetary Sciences Department, MIT, Boston, Massachusetts, U.S.A.

**Department of Earth and Environmental Science, University of Pennsylvania, Philadelphia, Pennsylvania, U.S.A.

††Department of Earth and Planetary Sciences, Macquarie University, NSW, Australia

‡‡School of Earth, Atmosphere and Environment, Monash University, Melbourne, Victoria, Australia

Key words. EBSD, Cryo-SEM, Ice.

Summary

Electron backscatter diffraction (EBSD) on ice is a decade old. We have built upon previous work to select and develop methods of sample preparation and analysis that give >90% success rate in obtaining high-quality EBSD maps, for the whole surface area (potentially) of low porosity (<15%) water ice samples, including very fine-grained (<10 μm) and very large (up to 70 mm by 30 mm) samples. We present and explain two new methods of removing frost and providing a damage-free surface for EBSD: pressure cycle sublimation and 'ironing'. In general, the pressure cycle sublimation method is preferred as it is easier, faster and does not generate significant artefacts. We measure the thermal effects of sample preparation, transfer and storage procedures and model the likelihood of these modifying sample microstructures. We show results from laboratory ice samples, with a wide range of microstructures, to illustrate effectiveness and limitations of EBSD on ice and its potential applications. The methods we present can be implemented, with a modest investment, on any scanning electron microscope system with EBSD, a cryostage and a variable pressure capability.

Introduction

Water ice microstructures provide insight into grain-scale processes such as grain growth, creep, fracture, recovery and recrystallization that are important in terrestrial ice systems including glaciers and ice sheets (Joughin *et al.*, 2005; Cuffey & Paterson, 2010; Gagliardini *et al.*, 2013; Faria *et al.*, 2014b; Montagnat *et al.*, 2014), sea-ice (Gough *et al.*, 2012), snow and firn (Spaulding *et al.*, 2011; Riche *et al.*, 2013). Microstructures can also help us understand the internal dynamics of and phase transformations within icy moons of the outer solar system (Poirier, 1982; Durham *et al.*, 2010) and phase transformations in Earth's upper atmosphere (Whalley, 1981; Riikonen *et al.*, 2000; Murray *et al.*, 2005). The creep behaviour of ice and associated microstructures also serves as analogues for processes in rock-forming minerals (Wilson *et al.*, 2014). Water ice plays a pivotal role in sample preparation for electron microscope investigation of biological tissues (McDonald & Muller-Reichert, 2008) and artefact-free tissue preservation is strongly dependent upon the ice microstructure that develops. Crystallographic preferred orientation (CPO) data are of particular importance in ice microstructure data sets as ice Ih has strong plastic (Budd & Jacka, 1989; Duval & Castelnau, 1995; Godert & Hutter, 1998; Cuffey & Paterson, 2010; Duval *et al.*, 2010), elastic (Harland *et al.*, 2013) and growth-rate (Rozmanov & Kusalik, 2012) anisotropies. Quantitative microstructural maps that show the spatial distribution of crystal orientations (Sander, 1970) are thus of extreme scientific value in the analysis of ice. Such data have been accessible for coarse-grained ice for decades: cross-polarized transmitted light images show ice microstructures and universal stage (Wilen *et al.*, 2003) measurements provide point measurements of ice *c*-axis orientations. More recently, automated fabric analyzers (Wilen *et al.*, 2003; Wilson & Peternell, 2011) have made such measurements much easier and faster. X-ray approaches using Laue diffraction (Miyamoto *et al.*, 2011; Weikusat, Miyamoto *et al.*, 2011) are also applied to coarse-grained samples. Other methods, including x-ray (Montagnat *et al.*, 2003) and neutron diffraction, on deuterated water ice (McDaniel *et al.*, 2006; Piazolo *et al.*, 2013), yield CPO data but lack a link to grain-scale microstructures.

Correspondence to: David Prior, Department of Geology, University of Otago, Dunedin, New Zealand. Tel: +6434795279; e-mail: david.prior@otago.ac.nz

The initial motivation for the work presented in this paper was to characterize the microstructures of fine-grained ice, with grain sizes between a few and a few hundred micrometres. Fine-grained ice samples are essential to explore grain size-sensitive creep and grain-growth behaviour over practical laboratory time scales (Goldsby & Kohlstedt, 1997; Azuma *et al.*, 2012). Many of the methods listed in the previous paragraph are difficult to apply to fine-grained ices, so we looked to electron backscatter diffraction (EBSD), the dominant method for quantitative microstructural analysis of metals (Humphreys, 1999; Schwartz *et al.*, 2009), ceramics (Saylor & Rohrer, 1999; Peruzzo *et al.*, 2011) and rocks (Prior *et al.*, 1999, 2009), as a means of mapping ice microstructures. Modern EBSD systems can measure grids of crystal orientations very rapidly with step sizes (grid spacing) as small as 50 nm. EBSD has been applied to coarse-grained ice samples for a decade (Iliescu *et al.*, 2004; Obbard *et al.*, 2006; Piazolo *et al.*, 2008; Montagnat *et al.*, 2011; Weikusat, De Winter *et al.*, 2011) but we discovered that published methods needed some development for routine application to fine-grained ice samples.

This paper presents the outcome of several years of technique development to make EBSD mapping of water ice routine and reliable, particularly for fine-grained laboratory ice samples. Laboratory samples typically represent significant investments of time and money, and are often critical components of research, so it is important to have analytical methods with a low failure rate. The principal author initiated this work by visiting the Stockholm (Piazolo) and Dartmouth (Obbard, Daghlian and Baker) laboratories to observe ice EBSD practices. Initial developments were made on extended visits to the Dartmouth Laboratory (Prior, Obbard, Diebold, Daghlian and Baker) in 2010 (Prior *et al.*, 2012). Further technical developments have been made at the Otago laboratory (Prior, Lilly, Easingwood, Seidemann, Vaughan and Becroft) between 2012 and 2014. We have tested and modified approaches using a wide range of laboratory ice samples from our laboratory (Prior, Becroft, Seidemann and Vaughan) and those brought by visiting teams (2013–2014) from the United States (Durham, Golding, Caswell, Goldsby) and Australia (Piazolo, Wilson). Between January 2013 and May 2014, we examined 94 different water ice samples with a >90% success rate. Here, we present a small subset of these data to demonstrate the effectiveness and limitations of our techniques. More complete data sets will be published in the future in the context of individual scientific investigations. The work presented here is applicable to low porosity (<15% porosity) water ice and includes discussion of the microscopy and preparation methods. Readers interested in the potential value of EBSD in ice research should skip to the section entitled "EBSD on water ice". The preceding material outlines the methods in sufficient detail that they can be applied in other laboratories.

Materials and methods

Effective EBSD mapping requires a damage-free surface with low curvature (ideally planar) that is free of topography at the scale of the features to be mapped. The sample surface is inclined at a shallow (~20°) angle to the electron beam (for a vertical column, samples are tilted to 70°) with no objects in the path between the sample and the EBSD camera. Sample surface charging must be avoided.

EBSD sample preparation for metallic and ceramic samples typically involves mechanical polishing to gain a flat surface followed by chemical etching, electropolishing, chemical-mechanical polishing or ion beam polishing to remove the Bilby layer (Lloyd, 1987) of defects created by mechanical polishing. The procedures developed for ice mirror this sequence. A special consideration for ice is that the surface of the sample must be free of frost.

Samples

All the samples discussed in this paper are synthetic; fabricated from pure deionized (unless stated) water. Samples include:

- *Standard Ice*: made by packing 180 to 250 μm sieved ice particles to ~40% porosity in a mould, evacuating air from the pore spaces, introducing outgassed water at 0°C and freezing from the bottom up (Stern *et al.*, 1997). Standard Ice has no porosity and a homogenous foam texture with mean grain size of ~0.5 mm (log normal distribution).
- *Wilson Ice*: made by mixing 180 to 250 μm sieved ice particles with water at 0°C. The majority of air bubbles are mechanically removed and excess water removed by lightly compressing the sample prior to freezing (Wilson & Russell-head, 1982). Unannealed Wilson ice has a heterogeneous structure. Annealing for several weeks at −8°C gives a low porosity ice with a mean grain size ~0.5 mm (log normal distribution).
- *Goldsby (Seed) Ice*: made by packing sieved ice particles to 40% porosity then pressing them hydrostatically with ~100 MPa of pressure at −78°C (temperature of dry ice). Porosity is low (<1 vol%) and final grain size closely reflects the initial particle size distribution.
- *Triple Drop Ice*: made by cycling Standard Ice through the ice Ih to ice II phase transformation three times (Stern *et al.*, 1997). Triple drop Ice has a slightly heterogeneous structure with a mean grain size of 10 to 20 μm.
- *Particle-Bearing Ice*: made by mixing ice particles with particles of harder materials prior to processing through one of the routes listed above. Particulates include graphite, alumina and calcite.
- *Columnar Ice*: grown by sprinkling snow onto ~0°C tap water in a bucket (insulated on all sides but the top) in a freezer. Columnar grains grow from the top surface and are typically >5 mm in diameter and >20 mm in length.

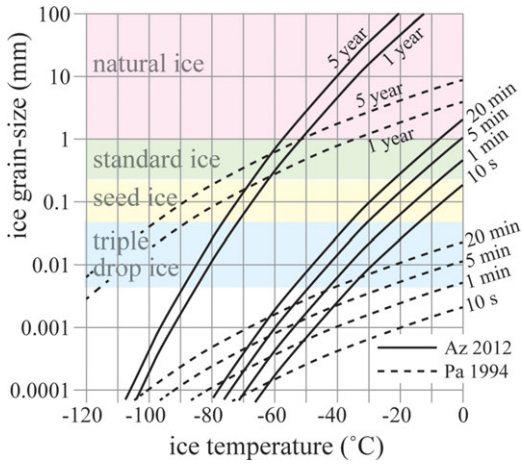

Fig. 1. Graph to show the temperatures for a given time (labels on curves) that will give 1% grain growth for samples of different grain size. Calculations (section 1.2) are shown for normal grain growth of clean, bubble-free ice (Az: Azuma *et al.*, 2012) and natural (bubbly and dirty) ice (Pa: Cuffey & Paterson, 2010).

Thermal history, handling and storage of samples

It is important to document the thermal history during sample preparation and storage to assess (and minimize) the likelihood that the sample microstructure is modified prior to analysis. Microstructural modification can occur by surface energy- (curvature-) driven grain growth (normal grain growth, annealing), strain energy-driven recovery and strain energy-driven grain boundary migration. Thermal modification of microstructures will be more likely in fine-grained samples and samples with high strain energy. Figure 1 provides order of magnitude constraints on the temperature – time histories that will preserve microstructures. Curves on the figure are calculated using the mean-field normal grain-growth relationship (Evans *et al.*, 2001)

$$D_t^n - D_0^n = k_0 \exp(-Q/RT)t \text{ which rearranges with } (D_t = GD_0) \text{ to} \quad (1)$$

$$D_0 = ([k_0 \exp(-Q/RT)t]/[G^n - 1])^{(1/n)} \quad (2)$$

where D_0 and D_t are initial and final mean grain diameters, respectively, G is the growth factor (G = 1.01 is used for 1% growth) and T the temperature in Kelvin. Two data sets for grain growth are used. One relates to bubble-free ice (Azuma *et al.*, 2012) with a growth exponent (n) of 2, activation energy for grain growth (Q) of 113 kJ mol^{-1} and a pre-exponential (k_0) of 3×10^{17} mm^2 s^{-1} (in the T range 0°C to −40°C calculated from Fig. 5 in Azuma *et al.*, 2012). The second data set relates to a compilation of grain-growth estimates from glacial ice (in the T range −15°C to −50°C: Cuffey & Paterson, 2010) with n = 2, Q = 42 kJ mol^{-1} and k_0 = 1 mm^2 s^{-1}. The curves for bubble-free ice are likely to represent the fastest possible ice grain growth. Each curve on the figure shows the temperatures (T), which will cause 1% grain growth over the labelled time period.

For large grain sizes, the driving force for strain energy-driven boundary migration can be much larger than those derived from boundary curvature (Duval *et al.*, 1983; Humphreys & Hatherley, 1996) so that the rates of microstructural reorganization can be faster than those estimated for normal grain growth for that grain size. Faria *et al.* (2014b) discuss the role of different driving forces and mechanisms for grain boundary migration in ice and conclude that strain energy is a significant control on grain boundary motion in ice. At this stage, we have no simple way to include strain energy in our analysis and we take a pragmatic approach. Ice with a grain size less than ~10 μm is unlikely to develop high strain energies (Goldsby, 2006) and normal grain growth will dominate. The thermal effects on strongly deformed samples coarser than ~10 μm are estimated by considering them to have a grain size an order of magnitude smaller than they actually have.

Long-term sample storage options include commercial freezers (typically −15°C to −30°C), commercial low-temperature freezers (−80°C) and liquid nitrogen (LN) storage dewars (−196°C). The finest grained samples (section 1.1) require storage in an LN dewar (triple drop ice would grow 1% at −80°C over a year). Long-term storage of all samples used in this paper has been in LN dewars. Medium-term (up to 2 weeks) sample storage and transfer (intercontinental and on campus) has used LN 'dry shippers' (Taylor Wharton Cryo-Express). In the SEM laboratory, short-term (up to a few hours) sample storage and transfer is accomplished with a 200–300 mm deep polystyrene sample transfer box. Samples sit on an internal metal mesh tray in contact with an LN reservoir. Sample temperatures can be stabilized between −170°C and −50°C depending upon LN level. The box needs a lid so that the sample sits in dry nitrogen gas.

Sections 1.3, 1.4 and 1.5 will provide data on the thermal effects of key sample preparation steps. Temperature effect experiments were conducted on Standard Ice samples. A hobby drill was used to make 2-mm diameter holes for K-type thermocouples which were sealed-in by freezing water in the hole. Temperature was logged using a National Instruments thermocouple module controlled by LabView software.

Sample cutting

Samples are cut to size for mounting and imaging in the SEM. We use a scroll saw (fret saw: Fig. 2A) designed for precision cutting of wood, and a ring saw (Gemini PrecisionXT) with a sintered diamond blade (Figs. 2B, C) designed for ceramic tiles and rocks. The saws are operated in a cold room at −10°C to −15°C. Low sample temperature is maintained by keeping the sample much colder, in a sample transfer box, at all times between cuts. Polystyrene sample grips (Fig. 2C) minimize direct contact of the sample with gloved fingers or metal surfaces (at the cold room temperature). Guides made of marble (Fig. 2C)

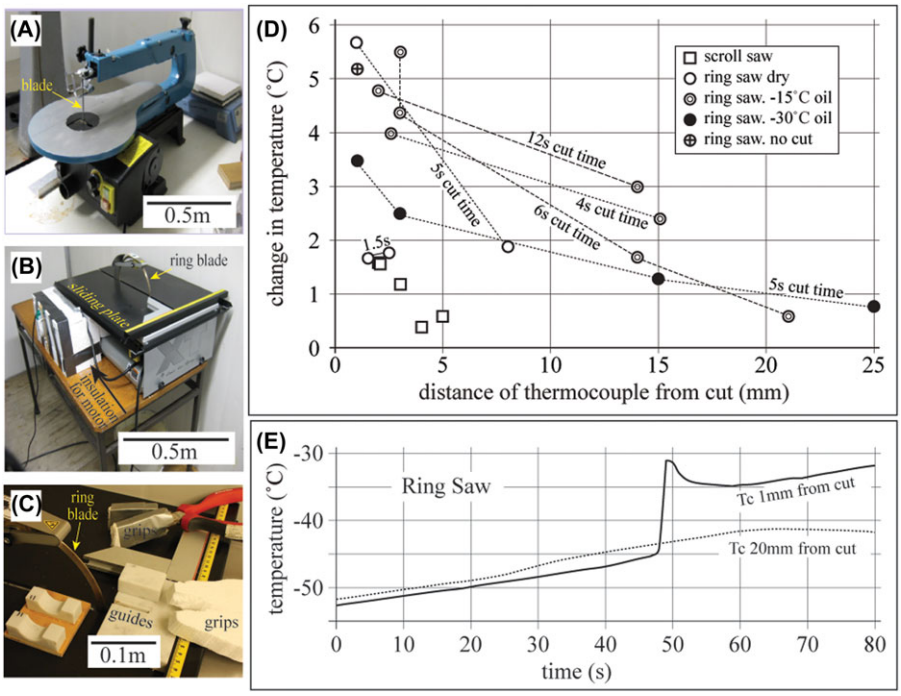

Fig. 2. Ice cutting tools and effects of cutting. (A) Scroll saw. (B) Ring saw. (C) Close up of ring saw blade with marble sample guides and polystyrene grips. (D) Summary graph of the thermal effects of cutting of samples with initial temperatures of ~−12°C. Lines link cuts of approximately the same duration. Cuts with oil have silicone oil as lubricant. In the 'no cut' test, a sample face was pushed against the stationary blade after the saw had run for ~10 s. Scroll saw thermal effects are not dependent on cut times in the range 1 to 12 s. (E) Thermal effect of cutting a "cold" sample with the ring saw in a cold room at −10°C. Background warming rate of ~10°C min^{-1} is believed to be a maximum – influenced significantly by conduction along the thermocouple wires.

that can be precooled to well below the cold room temperature are used to align samples for cutting.

The thermal effects of cutting samples with the scroll saw and ring saw are shown in Figures 2(D) and (E). Cutting routines that keep ice >1 mm from the cutting surface at temperatures that limit microstructural change to <1% are summarized in Table 1. At least 1 mm of material is removed by grinding the cut surface (section 1.5).

The ring saw is easy to handle, gives more precise and straight cuts and has a lower tendency to cause sample shattering than the scroll saw. Cutting is done without lubricant as the small advantage in cooling (Fig. 2D) is not worth the difficulty and mess involved. Extremely fine-grained, temperature-sensitive samples (e.g. triple drop ice) are cut with a scroll saw as the thermal effect is minimal. Highly fractured samples can be prepared without cutting, preparing flat faces by grinding alone (section 1.5). Samples that cannot be cut on the scroll saw (e.g. those with large or abundant hard particles) and that are too temperature-sensitive for the ring saw are cleaved/fractured to smaller sizes using a cold blade. A diamond wire saw cuts precooled (−80°C) ice and ice particle mixes easily (S. Piazolo): thermal effects are presumed to be less than the scroll saw but have not yet been quantified.

Sample mounting

A variety of mounting options for SEM analysis of ice (Erbe *et al.*, 2003) have been used in previous EBSD work. We have designed a copper sample mount, termed an 'ingot' hereafter, to which the sample is attached for surface preparation, imaging and storage. The design is simple, to allow us to fabricate many ingots. Samples remain attached to an ingot (and imaged multiple times) until no longer needed. The ingot is a 30-mm long copper bar with a trapezoidal section (Fig. 3A), which dovetails into the SEM cryostage (section 1.6). The ingot has a roughened top surface and several 3–4 mm vertical holes are drilled through from top to base. A threaded hole at one end allows the ingot to be picked up with a cooled bolt (with insulating handle). A phosphor-bronze leaf spring on the side of each ingot ensures good thermal contact at the base when mounted in the SEM cryostage. Standard ingots limit sample surface areas to 30 mm by 10 mm. Ingots with an additional plate brazed to the top surface (Fig. 3B) hold samples with surfaces up to 70 mm by 40 mm. Small samples are transported and stored in custom-made aluminium blocks ('toblerones': Fig. 3D) that have a triangular section and trapezahedral slots for the ingots.

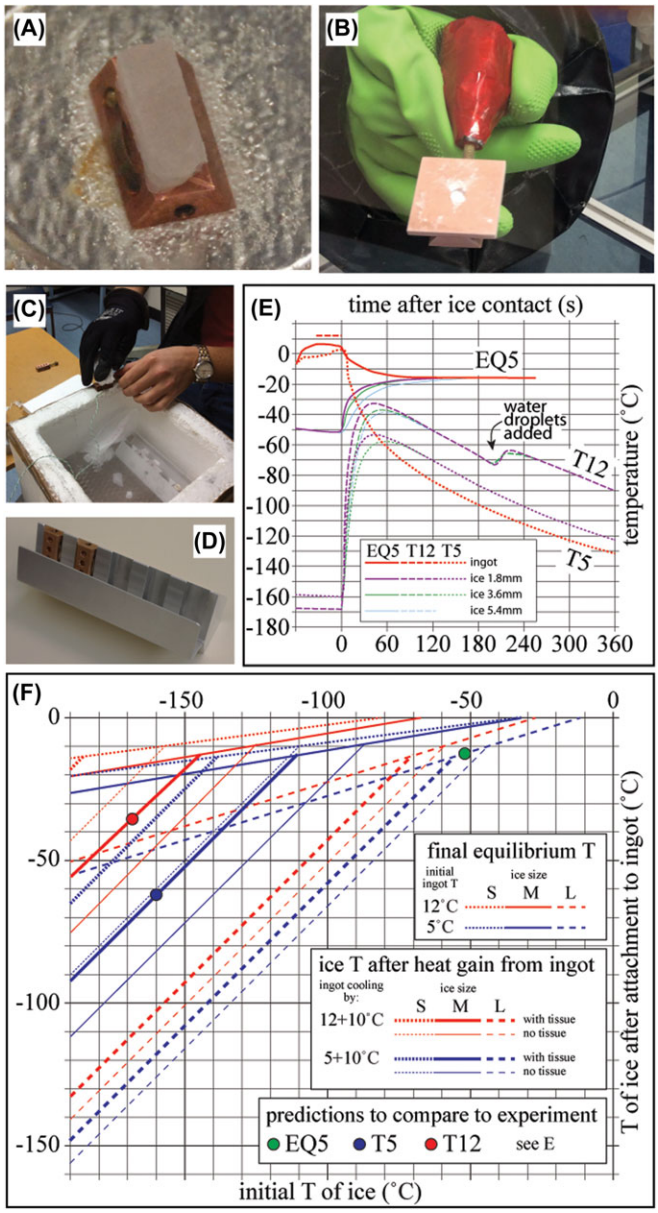

Fig. 3. Ice sample mounting. (A) Copper ingot (top: 30 mm by 10 mm) with ice sample. (B) Larger ingot (top: 30 mm by 30 mm). (C) Sample transfer box. Box contains LN to just below level of metal mesh. 'Toblerone' with mounted samples sits on the mesh. A sample is being mounted to an ingot on the rim of the box. (D) 'Toblerone' with ingots (no ice) in two slots. (E) Results of mounting experiments. Distances of thermocouples from the ice surface to be bonded are on the legend. Experiment EQ5 involved bonding a large sample (~30 mm × 10 mm × 10 mm) without tissue in an insulated box. Experiments T5 and T12 used the same medium-sized sample (~20 mm × 8 mm × 8 mm) bonded with a damp tissue. Sample was removed from cold transfer box (T < −160°C) immediately before bonding and returned there as soon as a firm bond was made. There is no ingot temperature record for T12, ingot was at 12°C at the moment of ice contact. Water droplets were syringed through the holes in the ingot base at t = 200 s in the T12 experiment. The thermocouples at 3.6 and 5.4 mm in the T5 experiment recorded the same temperature history. (F) Calculations (section 1.4) to help scale the thermal effects of melt-freeze attachment to different sample sizes and initial temperatures. Calculations are based on an ingot mass of 32 g and are made for small (S: 10 mm × 10 mm × 10 mm = 0.9 g, pecked line), medium (M: 20 mm × 8 mm × 8 mm = 1.2 g, solid line) and large (L: 30 mm × 10 mm × 10 mm = 2.7 g, dashed line) ice samples. Calculations use specific heat capacity values of 2005 and 386 kJ kg^{-1} K^{-1} for ice and copper, respectively, and a specific heat of water freezing of 334 kJ kg^{-1}. The shallower lines show resulting equilibrium temperatures if ice samples of different initial temperature are attached to ingots of 5°C (blue lines) and 12°C (red lines). The steeper set of lines simulate the mean maximum temperature the ice sample will reach as soon as a bond is formed (after which ice and ingot are cooled). The lines show the temperature the ice will reach if all the heat released by cooling the ingot by a fixed amount (from initial temperatures of 5°C and 12°C down to −10°C) is used in warming the ice. 'No tissue' calculations ignore the heat of melting/freezing. 'With tissue' calculations include the heat released in freezing a 0.5 mm thickness of water. Labelled dots show calculations that correspond to experimental results in (E).

Table 1. Guide to best cutting routines based on sample characteristics

Ice characteristics	Maximum T (for ice >1 mm from cut) for time outside transfer box – up to a few minutes	Precooling temperature (in transfer box)	RING saw applicability	SCROLL saw applicability
10 μm grain size (e.g. triple drop ice)	−60°C	−70°C to −80°C[b]	Very poor	Good
100 μm grain size (e.g. Goldsby (seed) ice)	−40°C	−50°C to −70°C	Poor	Good
500 μm grain size (e.g. Standard ice, Wilson ice)	−30°C	−50°C to −70°C	Good to excellent[a]	Good
>1 mm grain size (e.g. natural ice)	−20°C	−20°C to −70°C	Good to excellent[a]	Good
Fractured ice	Depends on grain size	Warmer than −50°C	Good	Poor
Ice–graphite mixes	Depends on grain size	Depends on grain size	Excellent	Good
Ice–alumina/calcite mixes with particles <1% and <1 μm	Depends on grain size	Depends on grain size	Excellent	Adequate
Ice–alumina/calcite mixes (large or abundant particles)	Depends on grain size	Depends on grain size	Good	Very poor

[a]Ring saw works better, with less fracturing, with warmer samples.
[b]Lower precooling temperatures increase chance of fracture. Colder than −80°C gives a high chance of shattering.

Sample mounting is based on melting and refreezing a thin layer of ice to make a bond with the copper ingot. The high heat capacity and low thermal conductivity of ice, compared to low heat capacity and high thermal conductivity of Cu, make it easy to melt and freeze a thin layer with minimal thermal impact on the samples.

In practice, the mounting procedure involves pushing very cold ice (~−160°C) against an ingot at a temperature above 0°C. As soon as a bond is made (ingot temperature ~−10°C), the sample is returned to the cold sample transfer box (~−160°C). A good bond can be achieved by this approach with a melt film significantly less than 1 mm thick. A modification of this approach, which has a higher success rate, is to use a piece of damp tissue (e.g. kitchen tissue) between ice and ingot. The ice sample (~−160°C) is placed on top of a damp tissue-coated ingot at a temperature above 0°C. The mounted sample is put back into the sample transfer box when the ingot cools below 0°C.

In practice, procedures with and without damp tissue can be tailored to ensure that no ice (more than 1 mm from the interface) exceeds a given critical temperature (defined using Fig. 1). Figure 3E shows temperature records from bonding experiments and Figure 3F shows the results of some simple thermal equilibrium calculations that can be used to guide procedures for different samples. The initial ingot temperatures and the medium and small sample sizes are chosen so that the calculations can be compared with the experiments shown in Figure 3(E).

Two types of calculation are shown in Figure 3(F). The first shows final equilibrium temperature (T_f) for ice and copper, with initial masses and temperatures M_I, T_I and M_{Cu}, T_{Cu} brought together with no external heat loss or gain. These calculations do not include heat of melting or freezing, as both should occur (and cancel out)

$$T_f = (C_{Cu}M_{Cu}T_{Cu} + C_IM_IT_I)/(C_{Cu}M_{Cu} + C_IM_I). \quad (3)$$

The second set of calculations simulates rapid cooling of the ingot after a melt bond is achieved. This is done by calculating the change in ice temperature (ΔT_I) assuming heat is lost from an ingot that cools (ΔT_{Cu}) from an initial temperature to a temperature below freezing (−−10°C is used here).

$$\Delta T_I = (\Delta T_{Cu}C_{Cu}M_{Cu}/C_IM_I) + (CF_wM_w/C_IM_I). \quad (4)$$

The second term relates to the freezing of a water layer in the tissue (CF_w = specific heat of fusion of water, M_w = mass of water). This term will be zero with no wet tissue.

In reality, ice warming and melting will be localized at the contact with Cu because of the low thermal conductivity of the ice, as can be seen in the response of the different thermocouples in Figure 3(D). Nevertheless, the calculations match the experimental results well and provide a framework to modify the procedures for different sample dimensions. Ice mass, ice and ingot temperatures, and the speed of cooling of the ingot after a bond is made are the most critical parameters (as can be seen from Fig. 3F). Bond strength tends to be better with higher ingot temperatures and ingot temperatures below 5°C often make no bond or only a weak bond.

Our current practice is to bond coarse-grained samples (e.g. standard ice) with an ingot temperature of 12°C, and samples with a grain size of ~10 μm with an ingot temperature of 5°C. Particular care needs to be taken with smaller samples as the low sample mass results in a larger temperature rise in the ice (Eq. (4). In smaller and/or more temperature-sensitive samples (e.g. ~1 μm grain size) as soon as the bond is made,

the ingot is pressed against another ingot at LN temperature. The temperature of the two ingots equalizes at about −100°C in a few seconds, reducing heat transfer to the ice sample.

After the sample is mounted, 0°C water droplets are injected by syringe into the holes at the back of the ingot to strengthen the bond. The temperature effect of this procedure is minimal (Fig. 3E).

Obtaining a flat surface

Three methods are available to prepare the sample surface: cryomicrotome, grinding and cleaving. The cryomicrotome is relatively easy and effective but has a thermal effect that might modify fine-grained microstructures. Grinding and cleaving methods have no significant thermal effect and work on samples with ice with hard particles, but do not produce as good a surface as the cryomicrotome.

We used a cryomicrotome with a refrigerated chamber (Fig. 4A) that can be cooled to −30°C. A desktop microtome used in a cold room (as used in making ice thin sections) would likely give similar results. A stainless steel D-cut blade is used. The cryomicrotome leaves marks on the sample surface (Figs. 4B, C) and if the blade is blunt, surface damage can be significant (Fig. 4B). Sample fracturing can become a problem below −40°C and samples (especially those with cracks or high porosities) need to be warmed (from the temperature in the transfer box) before shaving. It is impossible to use the cryomicrotome without the sample reaching the chamber temperature (−30°C). With practice, preplanning and good luck, the time spent at this temperature can be reduced to about 2 minutes: more commonly it will be 10 to 15 min. Use of the cryomicrotome is acceptable for ice with grain sizes $>100\ \mu$m. Care must be taken with ice of $\sim 10\ \mu$m grain size: Figures 4 (D) and (E) show an example of cryomicrotome-induced grain growth. The cryomicrotome can be used on mixtures of ice and graphite, but not on ice-alumina or ice-calcite mixes as the hard particles damage the blade.

A flat sample surface can also be obtained by grinding. The sample is polished on grinding paper on a metal plate cooled to −50°C to −80°C. The sample surface maintains a temperature equal to or below the grinding plate temperature. Grinding matches parallel procedures used in rock preparation (Fynn & Powell, 1979; Lloyd, 1987) following a sequence from 600 grit to 1200 grit, to 2400 grit, then (if needed) to 3 and 1 μm. Grinding can result in a sample surface that is neither perfectly flat nor perfectly parallel to the ingot. Very large samples (>30 mm wide) do not fit our microtome and need to be ground. Maintaining a flat surface on larger samples is easier.

An ice surface can be cleaved with a razor blade. Cleaving can produce locally flat surfaces (e.g. Fig. 4D), but the area available for EBSD may be restricted. Selecting a specific area of the sample for EBSD is difficult. With careful sample handling, the temperature impact of cleaving is insignificant.

Sample transfer into the SEM

Many commercial SEM cryostages are linked to cryotransfer systems. Sample preparation is carried out in a chamber that is external to the SEM vacuum chamber (an airlock) from which the sample is transferred directly into the SEM. Commercially available systems have significant disadvantages for cryo-EBSD. A restriction in preparation methods is a key problem; an equivalent of the cleaving method would be possible but no equivalent of the cryomicrotome or grinding methods are usually available. Some cryotransfer/-stage systems limit sample tilt or movement and none are designed for large samples.

Nitrogen-filled glove box. For maximum flexibility, we transfer the sample through the main chamber door of the SEM. We have built a nitrogen glove box that fixes over the chamber door and enables sample handling and exchange in a dry, clean gas atmosphere that reduces frost formation (on sample and on the cryostage).

The nitrogen glove box shown in Figures 5 (A) and (B) is custom-built for the Zeiss SEM. The box is constructed from clear Plexiglas and has two pieces. One piece (Fig. 5A) attaches behind the door seal of the SEM using gaffer tape. This piece has a slot to allow passage of power, control and monitoring cables. The cables need to move as the door opens and closes so a flexible seal is made from thin sheet rubber held in place with gaffer tape. The external LN reservoir, which is mounted on the door of the SEM, is filled through a hole in the Plexiglas, which allows LN entry (Fig. 5A). The port is sealed by a friction-fit plastic seal to minimize gas escape, and is covered by a lid for a tight seal when the chamber door is open and the LN reservoir moves (Fig. 5A).

The second (main) piece of the glove box (Fig. 5B) is wheeled into place and sealed to the first piece with a strip of 1 mm thick rubber and gaffer tape. A fold in the rubber seal isolates the SEM from any vibrations. The main glove box has several flexible arm access points, with150 mm flexible ducting attached to extra-large-size rubber gloves. The extra-large size allows the user to wear thin cotton gloves when handling very cold items in the glove box. A two-door access port in the base of the main glove box allows the sample transfer box and a selection of tools to be taken in and out with minimum gas exchange.

Humid air is purged from the glove box by warm nitrogen gas generated from a 50 L LN dewar and passed through ~3 m of coiled pipe in a bucket of hot water. The whole system is at positive pressure, rather than being very tightly sealed, which prevents backflow of humid air into the glove box. Major leaks and the two door access are near the base of the glove box: warming the nitrogen ensures it fills the space from the top down.

The cryostage used is an EMITECH K1250 cooled by conduction to an LN reservoir. The LN reservoir (~1.5 L), outside the chamber (Fig. 5A), cools a 20-mm diameter copper rod that passes through a feed through on the SEM door (Fig. 5C).

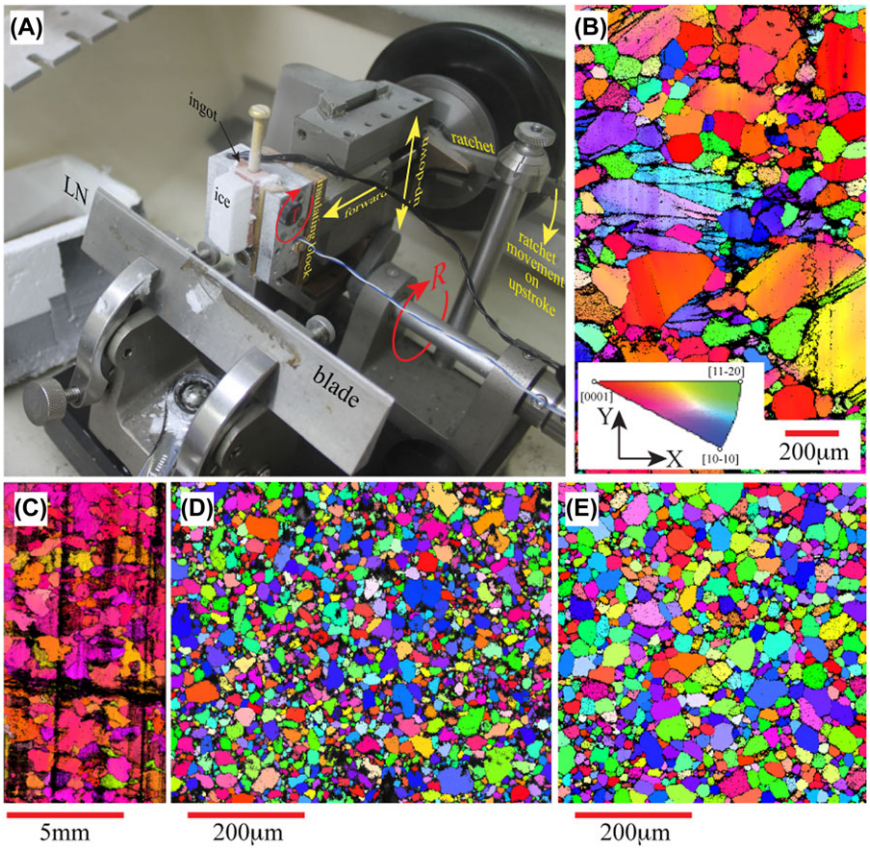

Fig. 4. Cryomicrotome equipment and effects. All EBSD data shown as IPF Y maps: colour shows the crystal orientation in the Y direction, as shown in the legend inset into B. Raw EBSD data: black pixels are unindexed. X-Y reference frame the same for all samples. All samples pressure cycle sublimed. (A) Cryomicrotome with mounted ice sample in place. Ingot fixed rigidly with hex-headed bolt (T). Photograph taken through upper hatch (open) in refrigerated tank. A wheel outside tank rotates (R) to effect up-down motion of sample. A ratchet is engaged on each upstroke to move the sample forward a fixed distance (2–16 μm). Shaving occurs on the downstroke. (B) EBSD map (2 μm step) of sample MIT748M2. Standard ice deformed at -43°C, 15 MPa differential stress and 50 MPa confining pressure to a strain of 0.37 (shortening parallel to Y). Large grains are deformed, smaller grains are undeformed and interpreted as recrystallized. Vertical lines of colour change are deformations induced by asperities on microtome blade. (C) Large area EBSD map (10 μm step) of sample OUJ1002. Standard ice deformed unconfined at -3°C, 0.7 MPa differential stress to a strain 0f 0.15 (shortening parallel to Y). Cryomicrotome was blunt and significant scratches are visible in the map. (D) EBSD map (1 μm step) of sample MIT666. This is a triple drop sample with geometric mean grain size of 11 μm. Surface was cleaved at low temperature with a razor blade. (E) EBSD map (1 μm step) of sample MIT666 that has been cryomicrotomed ($\sim$15 min at -30°C). Geometric mean grain size is 25 μm.

A thick braid of copper wires clamps directly onto the copper rod and links the rod to the stage (Fig. 5C). The stage is made of copper with an $Ni_{85}Cr_{15}$ alloy coat. It has an internal T-type thermocouple.

Setup and transfer procedures. The setup procedure for ice EBSD takes about 1 h. The cryostage is installed in the SEM, the SEM chamber pumped to high vacuum ($<\sim 10^{-3}$ Pa) and gas supply to the glove box turned on. Cryostage cooling starts 15 min later; the time for N_2 to purge air from the glove box. When the cryostage temperature is below -100°C (20–30 min), the chamber is vented to insert the sample. The sample is precooled in the transfer box (at $\sim -160^{\circ}$C), inside the glove box. A precooled screw handle is used to push the ingot and attached sample into the cryostage. The sample is washed with LN (to remove any thick surface frost) immediately prior to closing the SEM door and pumping the chamber to high vacuum. In a fast sample exchange, the temperature of the cryostage will not rise above -90°C.

Figure 6(A) shows the quantity of frost typical of a sample transferred without the glove box. In contrast, Figures 6 (B) and (C) demonstrate the improved surface quality of a sample transferred through the glove box. Success of the glove box approach in eliminating frost depends on a number of factors (ambient temperature and humidity for example). Sometimes a sample has no frost; more typically there is layer of frost sufficiently thin that the sample surface can be seen through gaps in the frost (Figs. 6B, C). Having a frost-free surface does not guarantee good EBSD data, however, as the sample surface may still be damaged. Sublimation removes the damage.

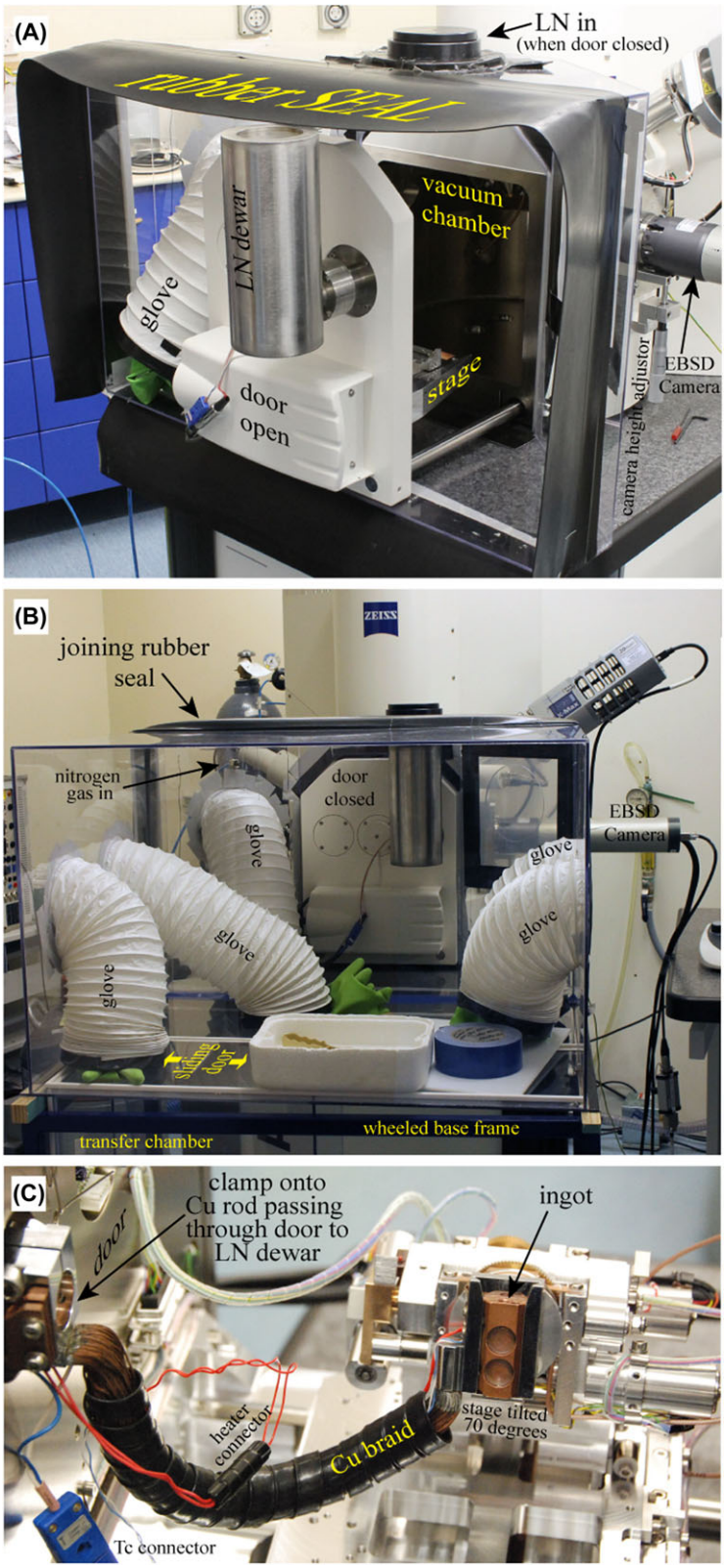

Fig. 5. Nitrogen glove box and cold stage. (A) Part of glove box that fixes to the SEM. SEM door opens into this. Rubber seal attaches to main glove box, using gaffer tape. (B) Main glove box attached to the part seen in A (behind – attached to SEM) by rubber seal and gaffer tape. Samples are brought into a transfer chamber through a vertical sliding door off the bottom right of the image and then up into the glove box through the horizontal sliding door marked. (C) View of cold stage in open door of the SEM. If chamber were closed, view would be from above EBSD camera. Stage tilted 70 degrees for EBSD.

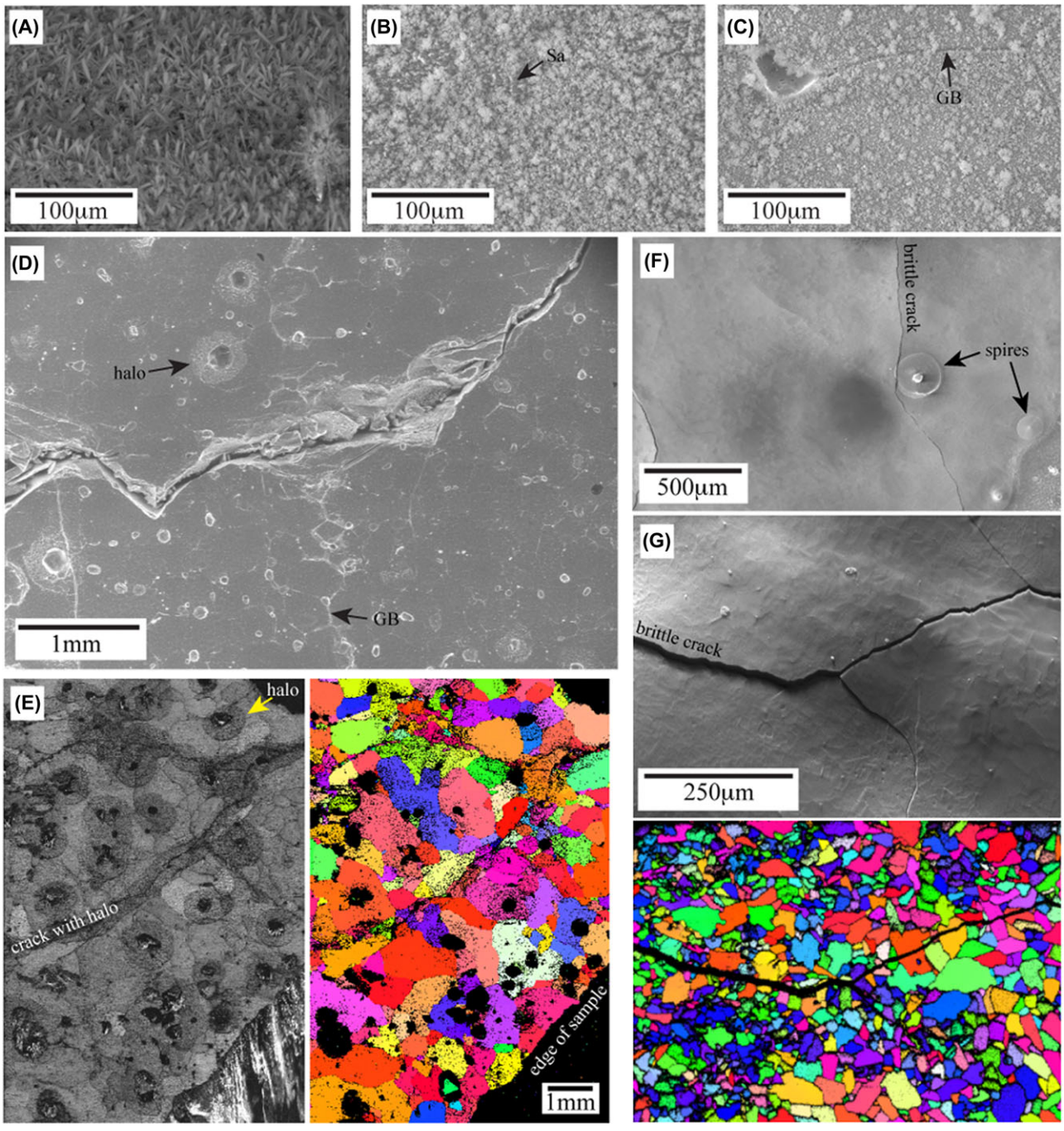

Fig. 6. Ice sample surfaces. (A) BSE image of bad frost on a sample that has passed through the lab atmosphere. (20 kV, ~10 nA, tilted 70°, WD = 19 mm) (B). VPSE image (15 kV, ~2 nA, flat sample, WD = 14 mm) of worst-case frost of sample inserted through N glove box. Small areas of sample surface (Sa) are visible. (C) VPSE image (15 kV, ~2 nA flat sample, WD = 14 mm) of typical frost cover of sample inserted through N glove box. Sample surface, including etched grain boundaries (GB) visible through frost. (D) VPSE image (15 kV, ~7 nA, flat sample, WD = 23 mm) of standard ice sample that has been pressure cycle sublimed. Etched grain boundaries (GB) are clear. Halos of precipitate (halo) occur around holes (plucked out grains). (E) Large area EBSD map (18.75 μm step) of sample MQMD6. This is Wilson heavy water ice deformed unconfined at -7°C, 6×10^{-7} s^{-1} strain rate to a strain of 0.1. Left-hand map (band contrast = pattern quality) shows precipitate around holes and cracks. Right-hand map (IPF Y map: see Fig. 4B for legend) shows that precipitate is in crystallographic continuity with underlying grains. (F) VPSE image (30 kV, ~15 nA, flat sample, WD = 19 mm) of deformed standard ice sample MIT722 that has been ironed. Each spire has a wide base and a needle like protrusion (up to a few hundred micrometres) perpendicular to the sample surface. Brittle cracks form during ironing. (G) Forescatter image and EBSD map (IPF Y map: see Fig. 4B for legend; 1 μm step) of triple drop ice sample MIT666 that has been ironed. Geometric mean grain size is 25 μm. Grains (topography) can be seen in the forescatter image.

Surface sublimation: removing frost and damage

Surface sublimation inside the SEM has been used to reveal ice microstructures (Cross, 1969; Stern *et al.*, 1997; Barnes *et al.*, 2002) through etching (due to different sublimation rates of differently oriented grains and at grain boundaries). Sublimation can also provide frost-free and damage-free surfaces for EBSD (Iliescu *et al.*, 2004; Piazolo *et al.*, 2008; Weikusat, De Winter *et al.*, 2011). Sublimation is conventionally achieved by warming the sample with a heater internal to the cryostage whilst the sample is under high vacuum. This proves effective for coarse-grained ice samples (op. cit.) but our attempts to use this approach with fine-grained ice have rarely been successful as the amount of material removed in sublimation is substantial (several micrometres to tens of micrometres, minimum), which creates surface topography on the scale of the grain size making EBSD indexing difficult or impossible.

The ice-vapour equilibrium line (Fig. 7) is crucial to understanding sublimation (Weikusat, De Winter *et al.*, 2011). The line shows the equilibrium water vapour pressure (P_{H20}) for a given ice temperature (T_i) and is calculated from the IAPWS formulation (Wagner & Pruss, 2002; Wagner *et al.*, 2011; Bielska *et al.*, 2013)

$$P_{H20} = P_{TP}\exp\left[\left(a_1\theta^{b1} + a_2\theta^{b2} + a_3\theta^{b3}\right)/\theta\right], \quad (5)$$

$$\theta = (T_i/T_{TP}). \quad (6)$$

P_{TP} is the equilibrium water vapour pressure at the H_20 triple point. $P_{TP} = 611.657$ Pa at a temperature $T_{TP} = 273.16$ K. Coefficient values are; $a_1 = -21.21$, $b_1 = 0.0033$, $a_2 = 27.32$, $b_2 = 1.21$, $a_3 = -6.11$, $b_4 = 1.70$ (Bielska *et al.*, 2013). Neither the older equilibrium relationship (Andreas, 2007) used in discussion of sublimation by Weikusat, De Winter *et al.* (2011) nor newer experimental data (Bielska *et al.*, 2013) differ by more than 2% from the IAPWS formulation shown in Figure 7.

Heating moves the ice temperature up at constant pressure, away from the ice-vapour equilibrium line (Fig. 7). At these conditions, the equilibrium vapour pressure of water is higher than the pressure maintained in the chamber. Sublimation occurs to raise the water vapour pressure and the SEM vacuum pump removes the vapour, reducing the pressure and stimulating further sublimation. The coldest object within a few centimetres of the sample is generally the sample itself (in detail, this depends on stage design), so no reprecipitation occurs near the sample. Since the pump action prevents water vapour pressure reaching equilibrium, sublimation is continuous whilst the temperature of the sample increases. Barnes *et al.* (2002) estimate sublimation rates of samples held at −80°C under high vacuum to be around 6 μm min^{-1} so it is easy to see how substantial material loss can occur. Because ice has a low thermal conductivity, a full sublimation cycle may often take more than 15 min.

We have developed two alternative methods for subliming the ice surface. As it is the surface that needs to be sublimed, both these methods were developed to heat the ice sample from the surface – rather than from inside. The 'pressure cycling' method relies on greater transfer of heat from chamber walls at higher chamber pressures. The 'ironing' method uses a heated surface in the vacuum chamber to flash sublime the sample surface.

Surface sublimation by pressure cycling. This method evolved from observing the effects of sample exchanges where the sample became very warm (−50°C) before pumping the chamber. Increasing pressure in the SEM chamber increases thermal exchange between the chamber walls and the sample and cryostage. Steady state stage temperature for our system is about −150°C at high vacuum (10^{-4} to 10^{-3} Pa), about −100°C with 15 Pa nitrogen gas pressure and about −30°C at 230 Pa.

The stage is allowed to cool to −100°C (at high vacuum) following sample exchange, before initiating a pressure cycle by venting the chamber with nitrogen gas and allowing the stage to warm, typically up to −65°C. The chamber is then pumped; pressure reduces rapidly to the high vacuum condition and the stage cools slowly. Figure 7 presents an example of a pressure cycle, annotated to show the time elapsed after venting the chamber. Five experiments, with ice and stage temperatures, and five with just stage temperatures, show the same pattern but are not plotted to maintain clarity.

During warming (0–300 s on Fig. 7), the water vapour pressure (P_{H20}) in the chamber rises in accordance with the equilibrium line. Although P_{H20} is orders of magnitude lower than the chamber pressure, sublimation occurs to allow P_{H20} to rise. We can estimate the mass of ice that will sublime, shown in Figure 7 as the thickness of ice lost from a sample. The number of moles (n) of water needed to achieve P_{H20} in a SEM chamber volume (V) is calculated using the ideal gas law

$$n = (VP_{H20})/(RT_C), \quad (7)$$

R is the gas constant and T_C the temperature of the chamber (and the water vapour). The molar mass ($M = 0.018$ kg mol^{-1}) and n give the mass of water vapour in the chamber and thus the mass (M_{SUB}) that needs to be lost by sublimation

$$M_{SUB} = nM. \quad (8)$$

The thickness of ice lost by sublimation (H_{SUB}) is calculated using the ice surface area (A) and the density of ice (ρ_{ice})

$$H_{SUB} = M_{SUB}/(\rho iceA). \quad (9)$$

The sublimation loss is a function of the sample temperature and dimensions. The sample is typically 5°C to 10°C colder than the stage (Fig. 7). The warmest temperatures observed in our cycles correspond to calculated sublimation losses of less than 1 μm (Fig. 7). On pumping, chamber pressure reduction

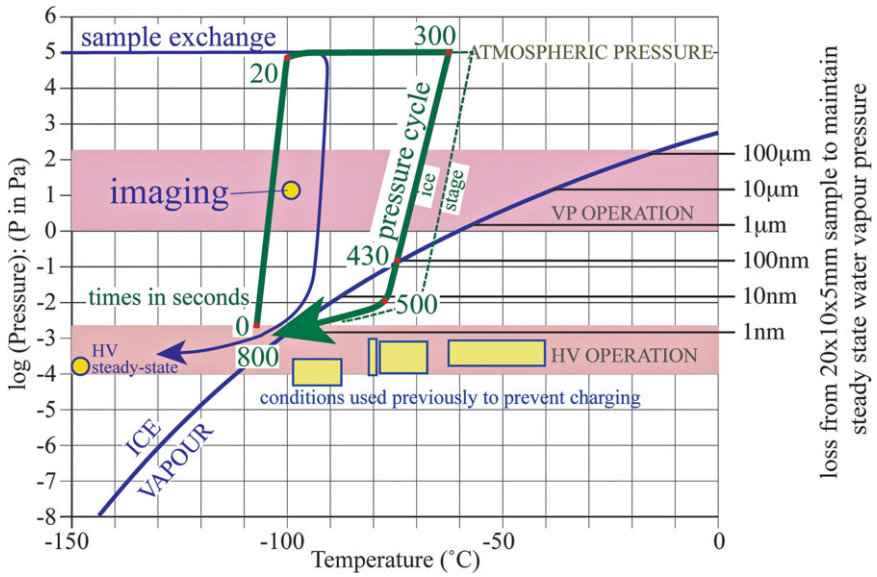

Fig. 7. Pressure–temperature diagram to explain sublimation procedures. The ice vapour equilibrium line (Wagner & Pruss, 2002; Wagner *et al.*, 2011) shows the equilibrium water vapour pressure for a given ice temperature. Previous EBSD investigations (squares: from Weikusat, De Winter *et al.*, 2011) used conditions where equilibrium vapour pressure is higher than chamber pressure so that samples continuously sublime and the water vapour close to the sample dissipates charge. Circles show steady state stage temperatures at high vacuum and in the VP mode (15 Pa) used for imaging and EBSD. Thin-line clockwise circuit shows the measured temperature of stage and chamber pressure during a typical sample exchange. Thick-line clockwise circuit shows the measured temperature of ice (~1 mm from imaged surface) and chamber pressure during a sublimation pressure cycle. A dashed line shows the cryostage temperature during the same cycle. Where dashed line cannot be seen, it lies under the ice PT line. Temperature error <1˚C. Uncertainty on log (P) at HV is ±0.3. Straight line sections between atmospheric pressure and ~10^{-2} Pa are interpolated (no P data). Scale on right-hand side shows the thickness of ice that would be removed by sublimation from a sample of 20 mm × 10 mm × 5 mm (five surfaces exposed) to generate the equilibrium pressure of water vapour (section 1.71) in the SEM chamber (V = 0.023 m^3). The thickness removed is a function of ice temperature and sample surface area and is relatively insensitive to chamber temperature.

occurs mainly in the ice stability field (from 300 to 430 s in Fig. 7). There is about 1 min of the pressure cycle (from 430 to 500 s in Fig. 7) where equilibrium P_{H20} is higher than chamber pressure and the rate of chamber pressure reduction greater than the rate of reduction in equilibrium P_{H20}. Maximum loss of water vapour into the pumping system and corresponding sublimation likely occurs in this short period. After this (from 500 to 800 s in Fig. 7), the rate of reduction of equilibrium P_{H20} is higher than the rate of reduction of chamber pressure; if pumping affects P_{H20} and P_{N2} equally, equilibrium P_{H20} is maintained with no need for sublimation.

The pressure cycle process removes remaining surface frost (Figs. 6B, C) and we infer that enough surface material (a few nanometres or more: Prior *et al.*, 1999) is removed to significantly improve EBSD. Generally, the loss of sample due to sublimation cannot be seen in secondary electron images; the preferential etching of grain boundaries exists prior to pressure cycle sublimation. Circular features that we presume are precipitates up to 0.5 mm in diameter surround some holes (plucked out grains) on the sample surface (Figs. 6D, E). We do not know the origin of these features and they do not generally interfere with EBSD indexing (Fig. 6E).

Target warming temperature will be higher for larger samples. Typical samples (20 mm by 8 mm by 8 mm) oversublime when the stage is warmed to −50˚C and sublimation can fail to remove frost when warming to −70˚C. These temperatures will likely be different for other SEMs/cold stages with different volumes, temperature control and pump rates; preliminary experiments on the system at Dartmouth College (T. Caswell, R. Obbard) show that samples are best warmed to only −80˚C. It is possible to get the pressure cycle effect by allowing the sample to get warm in sample exchange – this is current practice in the Montpellier laboratory (A. Tommasi; private communication).

Surface sublimation by ironing. This method evolved from attempts to heat the sample surface by radiation from a heater in the SEM chamber. Radiative heating was ineffective, but in a serendipitous accident, a sample touched the heater creating a good surface for EBSD. The ironing technique involves pushing a cold sample surface (<−130˚C) against a hot (~200˚C), polished zirconia plate; this is done at high vacuum. A thin layer of ice sublimes leaving a surface highly suited to EBSD analysis (Figs. 6F, G).

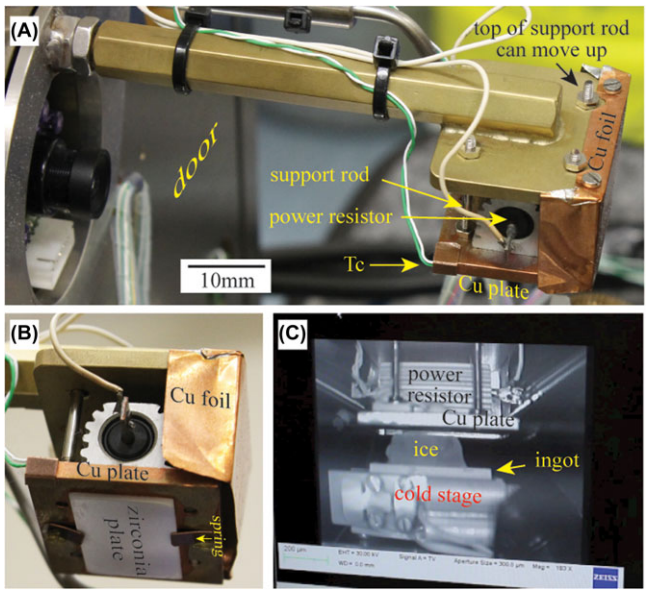

Fig. 8. Heater system used to iron sample surfaces. (A) Heater attached to SEM door, viewed from above. (B) View of zirconia plate on base of heater. (C) SEM chamberscope image of an ice sample attached to an ingot in the seconds before contact with the iron.

The heater comprises a power resistor (25 W 3.7 Ω) bolted to a 2-mm thick 20 mm by 30 mm copper plate (Fig. 8). A 0.6-mm thick 12 mm by 25 mm polished zirconia plate is attached to the copper with phosphor bronze springs and a smear of high temperature vacuum grease. The assembly is attached to the SEM door with the power resistor and plate hanging on support rods so that the heater lifts when pushed from below. A double layer of copper foil reduces radiation into the SEM chamber (Fig. 8). A K-type thermocouple is clipped to the copper. Power is delivered from a variable mains transformer.

Stage XY motion positions the sample under the heater (Fig. 8C) and Z movement advances the sample surface 50–100 μm higher than the contact point with the heater surface. Ten to 50 μm of sample surface is removed and a very slight upward movement of the heater is seen in the SEM chamberscope.

Zirconia has very low thermal conductivity so that only a thin surface layer will cool, minimizing heat transfer to the ice; the temperature of the copper plate does not change during the ironing. The cryostage does not change temperature during ironing. A thermocouple sensor in the ice, <1 mm from the sample surface, never shows a temperature increase greater than 2°C and usually shows a very small temperature decrease (~2°C), immediately following sublimation. This suggests that some heat is lost from the sample to fuel the sublimation, although most of the heat comes from temperature reduction of the zirconia. The heat for sublimation of a 10 μm layer (20 mm by 10 mm) can be generated by reducing the temperature of a ~30 μm layer of zirconia from 200°C to −130°C. Initial sublimation will isolate the ice from the heater so that continued sublimation extracts heat from the ice; sublimation of a 10 μm layer would decrease the temperature of a 20 mm by 10 mm by 10 mm sample by 1.4°C. Sublimation loss of 10 to 50 μm from a typical sample (20 mm by 10 mm area) corresponds (using the Eqs (7)–(9)) to a pressure increase of 10–50 Pa, a change that should trigger the vacuum interlock on the SEM chamber (preventing HV operation). The interlock is rarely triggered, suggesting the vapour reprecipitates locally.

The quality of the sample surface after ironing depends on how flat it was to start with and how precisely parallel the ice and zirconia surfaces are. Ironed surfaces are often very smooth (Fig. 6F). Sometimes the surface level and orientation varies between grains (Fig. 6G) although preferential etching of grain boundaries is rare. Brittle fracturing of the sample as it touches the heater is observed in chamberscope images and these fractures are visible on the sample surface (Figs. 6F, G). EBSD patterns are excellent and ironed surfaces areas can give close to 100% indexing (Fig. 6G).

Some artefacts of the ironing process are left on the sample surface. An undulation with a wavelength of a few millimetres and amplitude of a few micrometres is often visible in forescatter images (Fig. 6G). Precipitates on the sample surface have the same orientation as the underlying ice (Fig. 6G). Spire-like towers (Fig. 6F) are spaced across an ironed surface. High axial ratio grains at the edge of samples (Figs. 9A, B) are clearly artefacts. These grains are likely to be reprecipitation of water vapour on cold surfaces. The spire-like towers are thought to have a similar origin. Figures 9(C–F) shows the results of experiments designed to generate artefacts. Growth of ice into holes includes growth with a topotactic relationship to ice in the samples as well as growth with new orientations.

We have compared the microstructures in ironed and pressure cycle sublimed surfaces in eight samples. Microstructures that were not already recognized as artefacts in ironed samples are very similar to microstructures in the pressure cycled samples. Because of the material loss in ironing, we cannot examine exactly the same surfaces by the two approaches. Approximately 15% of ironed samples exhibited sufficient artefacts that the analyses were dismissed. In some cases, excessive artefact generation clearly correlates to surfaces which are not initially flat (Figs. 9D, F) or not ironed parallel.

Pressure cycling versus ironing. Of the 94 samples, 53 were prepared with pressure cycle sublimation, 27 by ironing, 8 by both and the remainder without a sublimation process. In general, we prefer the pressure cycle sublimation approach. It is more reliable and faster and does not generate artefacts. Ironing is only applicable to samples smaller than the zirconia plate and works best on the smallest samples. Ironing is not applicable to porous samples or samples with a second phase. We maintain the ironing capability as there are some very

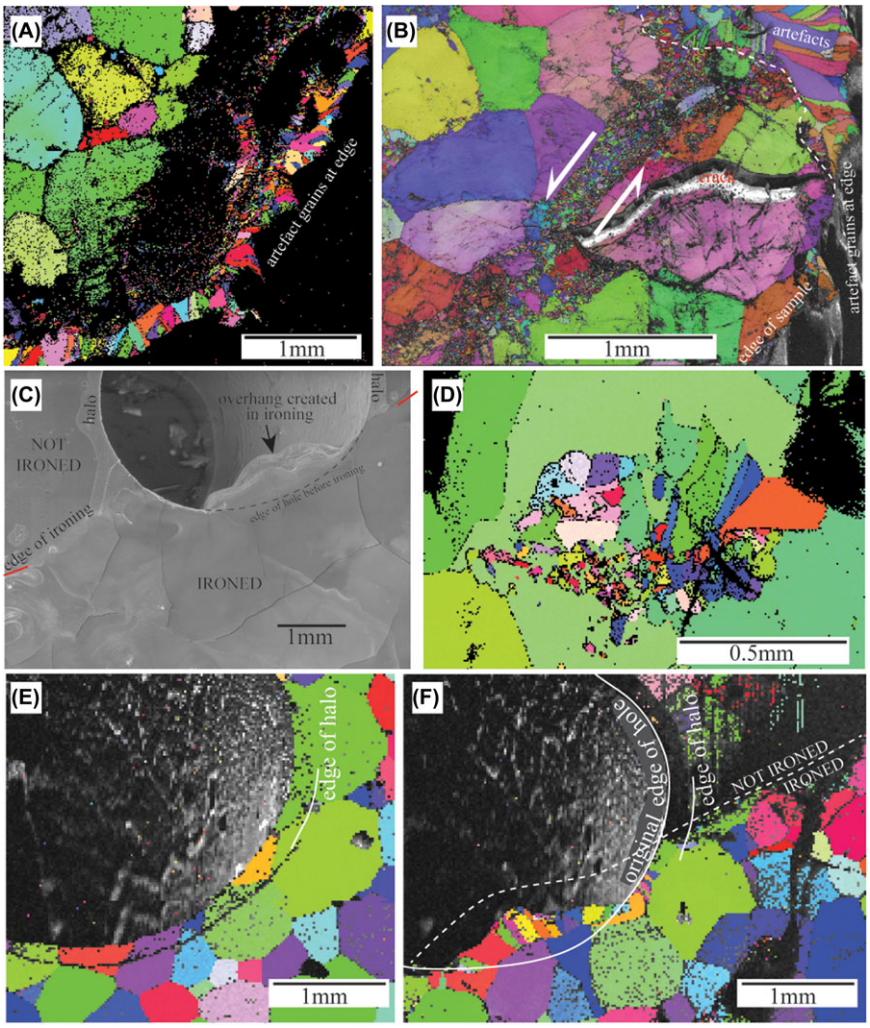

Fig. 9. Artefacts induced by Ironing. (A) EBSD IPF Y (see Fig. 4B for legend) map (10 μm step) of sample MIT722. Sample is standard ice deformed at -53°C to a strain of 0.22 (shortening direction unknown: sample fragmented). Elongate grains along the edge of the sample are artefacts, from vapour transport and precipitation of material removed by ironing. Area of poor indexing between real and artefact microstructures is of uncertain origin. (B) EBSD IPF Y (see Fig. 4B for legend) map (5 μm step) of sample MIT730. Standard ice deformed at -78°C, 3×10^{-3} s^{-1} strain rate and 50 MPa confining pressure. Shortening is vertical (parallel to Y). A zone of localized shear occurs between the shear arrows. Grains outside the shear zone are internally distorted (colour gradients). Fine grains in the zone of localized shear comprise a mixture of small, deformed grains, with similar orientation to larger grains in the shear zone wall, together with small undeformed grains with random orientations, interpreted as recrystallized. Artefacts correspond to sample edge. (C) VPSE (15 kV, ~10 nA, flat sample, WD = 19 mm) image of standard ice sample, with a 4 mm hole, used for an ironing artefact test. Halos around the hole formed during pressure cycling, prior to ironing. Iron and sample surfaces were not exactly parallel so that an edge of the ironed surface passes from bottom left to top right. Ice overhanging the edge of the hole was created during ironing. Brittle cracks in the ironed area formed during ironing. (D) EBSD IPF Y (see Fig. 4B for legend) map (5 μm step) of an area imaged from just below the area shown in C. The fine grains are artefacts that correspond to a small depression in the surface prior to ironing. (E). EBSD IPF Y (see Fig. 4B for legend) map (5 μm step) of part of the area shown in C. Map made after pressure cycle sublimation but before ironing. Halo around the drill hole gives crystal orientations contiguous with grains outside the halo. (F). EBSD of the same area (approximately) as shown in E, after ironing. The overhang comprises some grains that have the same orientation of original grains and some entirely new grains. An area of poor indexing occurs next to the edge of ironing.

small samples that cannot be pressure cycled and ultimately the very best EBSD data (highest indexing) come from ironed samples. If we manage to prepare ultrafine samples (grain size <1 μm), ironing may give much better data because of the lack of etching of grain boundaries.

Image and EBSD acquisition and data processing

All electron microscope data presented in this paper were collected on a Zeiss Sigma VP FEGSEM at the Otago Centre for Electron Microscopy. The instrument is used in a high current mode that also gives a very good depth of field. All imaging

and EBSD is conducted in variable pressure mode usually with 15 Pa of nitrogen as process gas. Samples are maintained at close to −100°C under these conditions. Equilibrium vapour pressure is much lower than chamber pressure and in practice samples can be imaged for several hours with no sublimation or precipitation.

Secondary electron images use accelerating voltages between 5 and 30 kV and beam currents between 0.1 and 90 nA. All EBSD data are collected at 30 kV with ~90 nA of current. EBSD data are collected using a NordlysF camera. EBSD patterns are acquired, processed and indexed using the AZTEC software (Oxford Instruments, High Wycombe, UK). In many cases, the patterns are stored. Working distances between 16 and 45 mm have been used, the EBSD camera being moved vertically (height adjustor shown in Fig. 5A) to maintain approximately the same pattern centre. The camera position corresponds to capture angle of ~120°. The camera is used at a 2 × 2 binning level at the highest gain, usually adding two to four frames to reduce noise. EBSD data acquisition and indexing is at rates between 60 and 180 patterns per second. Large area mapping involves using stage movement to stitch together (with 10% overlap) individual areas analyzed by beam scanning. Figures for this paper were created using AZTEC, the Channel software from Oxford Instruments and the Matlab toolbox MTEX (Bachmann *et al.*, 2010). All EBSD data are presented in a raw, unprocessed form.

EBSD data from water ice

Fine-grained ice

The ability to work on fine-grained ice samples opens a range of scientific opportunities. Sample MIT666 (Figs. 4D, E; 6 G) is a triple drop sample and has grain shapes, CPOs, misorientations and grain size distributions comparable with a much smaller data set used by Prior *et al.* (2012) to constrain the nature of the ice 1h to ice II phase transformation. Cryo-EBSD enables us to design programmes to analyze this and other ice transformation mechanisms at high pressure (e.g. ice II, III, V, IX) and low temperature (e.g. Ice 1c). The H_20 has a very rich phase diagram (Salzmann *et al.*, 2011) and a better understanding of phase transformations in this system is likely to yield more general insight into materials phase transformations.

Dynamically recrystallized grains are often finer-grained than parent grains in a deforming crystalline material (Urai & Jessell, 2001; Law *et al.*, 2010; Stipp *et al.*, 2010; Golding *et al.*, 2012). Figures 4(B), 9(B) and 11(A) all show finer grains generated during creep. Cryo-EBSD allows us to examine the crystallographic relationships of the parent and recrystallized grains (Bestmann & Prior, 2003) to help understand better the recrystallization process. Such studies are important for the general understanding of recrystallization: ice 1h has no known twins so data from ice, along with a relatively limited range of other materials (olivine, garnet), help us understand recrystallization isolated from twinning mechanisms that may be incorporated into the recrystallization process (Lloyd, 2004; Field *et al.*, 2007) in other materials (e.g. FCC metals, calcite, quartz, plagioclase, pyroxene).

Grain size distributions in ice have their own significance. Creep of finer grain size ice will have a larger contribution from grain size-sensitive mechanisms (Goldsby, 2006; Faria *et al.*, 2014b): the rheology of ice will vary with grain size. Grain size-sensitive rheologies can be constrained in the laboratory and there is evidence of involvement of these rheologies in ice sheets (Cuffey & Kavanaugh, 2011) and the interiors of icy moons in the outer solar system (Barr & McKinnon, 2007; Durham *et al.*, 2010). Furthermore, a composite rheology that involves both grain size-sensitive and grain size-insensitive flow laws (Goldsby, 2006) fits natural data. The limitation in understanding fully the significance of grain size-sensitive rheologies, particularly in terrestrial ice sheets, relates to poor constraint on the kinetics of grain size reduction during recrystallization and static grain growth. The piezometer relationship between the magnitude of differential stress that drives creep and the grain size (Twiss, 1977) is recognized in ice (Jacka & Jun, 1994) but is limited by the narrow range of recrystallized grain sizes reported. Ice EBSD enables us to constrain microstructural evolution in experiments and impose better constraints on the kinetics of grain size change. A combination of confined medium experimental methods (Durham *et al.*, 1987; Samyn *et al.*, 2014) and cryo-EBSD gives scope to extend this relationship to higher stresses and finer grain sizes and to reduce significantly the uncertainty in the piezometer.

Grain-growth kinetics have a significant impact on grain size evolution during creep (De Bresser *et al.*, 2001; Austin & Evans, 2007) and have always been recognized as significant in the microstructural evolution of ice sheets (Alley *et al.*, 1986, 1987). Constraints on grain size kinetics have been limited by a narrow range in grain sizes used in experiments and from natural systems (Alley *et al.*, 1986). By far the best kinetic data on ice grain growth have come from recent experiments that use a fine-grained starting material (Azuma *et al.*, 2012), using a sublimation etching method to see grain boundaries. Interaction with bubbles and particles is clearly important in natural terrestrial ice (Azuma *et al.*, 2012; Faria *et al.*, 2014b; Roessiger *et al.*, 2014) and further experiments are needed. Incorporation of cryo-EBSD into these experimental approaches gives another way to constrain grain size evolution and has the added value of showing how grain-growth processes may be influenced by grain boundary crystallography (Rohrer *et al.*, 2004; Rohrer, 2011).

Ice with hard particles

Much of the ice in natural ice masses contains particles of much harder material (minerals and rock). This is true for the

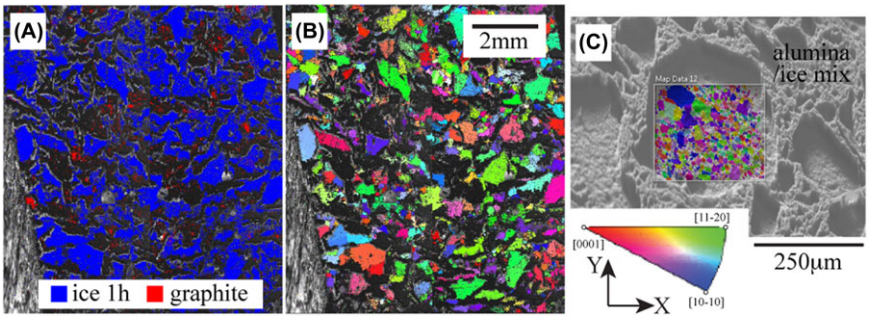

Fig. 10. EBSD data for samples with ice mixed with a hard phase. All samples prepared by pressure cycle sublimation. (A) Large area EBSD (Phase) map of sample MQG09, a D_20 graphite mix (20 vol% graphite), deformed unconfined at $-7^{\circ}C$, 2.5×10^{-6} s^{-1} strain rate to a strain 0.1. Uncoloured pixels are not indexed: most correspond to graphite. (B) EBSD IPF Y (see C for legend) map of the same area as shown in A. Only ice solutions are coloured. (C) Ice alumina mix prepared by mixing triple drop ice with 20%, 300 nm alumina. EBSD IPF Y map (1 μm step) superposed on VPSE image that shows the distribution of the alumina. Sample comprises a web of well-mixed alumina and ice with ~250 μm pure ice inclusions

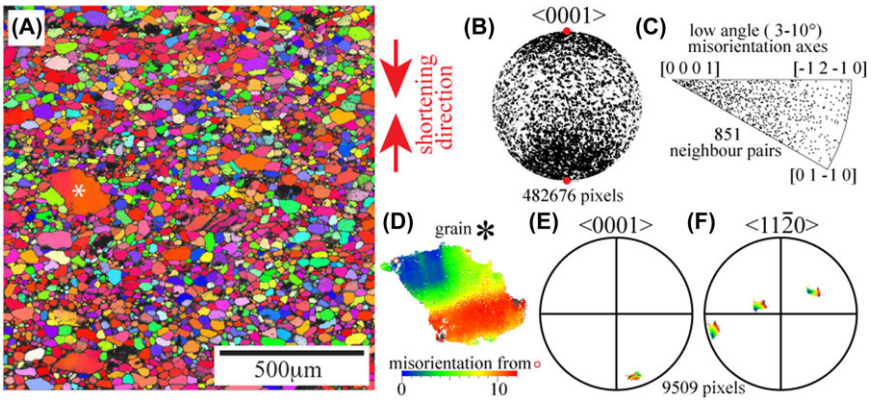

Fig. 11. CPO and distortion data from EBSD maps. (A) EBSD IPFY (see Fig. 4B for legend) map (1.5 μm step) of sample MIT748M1. The sample is seed ice deformed at $-43^{\circ}C$, 15 MPa differential stress and 50 MPa confining pressure to a strain of 0.37. (B) Stereonet to show *c*-axis (<0001>) pattern for the whole sample. (C) Low angle neighbour pair (Wheeler *et al.*, 2001) misorientation axes. (D) Detail of a large grain (marked * in A), coloured by the misorientation angle from the orientation at a marked point (circle) within the grain. Scale twice A. (E) Stereonet to show *c*-axis (<0001>) pattern in the grain in D. (F) *a*-axis (<11–20>) pattern.

basal zones of terrestrial ice sheets (Macayeal, 1989) and is a particular focus for understanding extra-terrestrial ice systems (Durham *et al.*, 1992; Barr & McKinnon, 2007).

Figure 10 shows preliminary ice EBSD data from samples that contain graphite and alumina. In the ice-graphite sample (Figs. 10A, B), the graphite also yields EBSD patterns (although indexing rates on these are low: <10%), suggesting that simultaneous analysis of ice and the hard phase may be possible. Some data suggest this may also be possible with mica as a hard phase (Obbard *et al.*, 2011).

Sample data from an ice/alumina mixture (Fig. 10C) illustrate the ongoing need to improve sample preparation approaches. The sample comprises ~0.5 mm clasts of polycrystalline ice in a matrix of fine ice alumina (300 nm) mix. There is significant difference in topography between the alumina-rich and alumina-poor regions, presumably related to differential sublimation before or during sample exchange. These samples cannot be prepared by the ironing method.

Large ice samples

Natural terrestrial ice samples tend to be very coarse-grained. Glacial ice has grain sizes in excess of a few millimetres (Alley & Woods, 1996; Bentley & Koci, 2007; Binder *et al.*, 2013) and sea ice has columnar grains tens of millimetres in diameter and up to metres in length (Gough *et al.*, 2012). Representative microstructural data from natural ice needs big samples. The grain boundary microstructures of very large ice samples can be analyzed using sublime etching and reflected light (Binder *et al.*, 2013; Faria *et al.*, 2014a); this approach can be used for continuous characterization of an entire ice core. Usually, *c*-axis fabrics of large samples are collected in transmitted light analysis of thin sections. Although *c*-axis data show the development of CPO, full misorientation analysis is not possible. The misorientation data help in interpretation of deformation, recovery and recrystallization mechanisms. Figures 11A, B show a deformed sample where the internal distortion of grains (3–10 degree misorientation axes) are

dominated by rotation around the *c*-axis. These data are impossible to collect with an optical method and allow an analysis of the geometrically necessary dislocations responsible for distortion (Lloyd *et al.*, 1997; Prior *et al.*, 2002; Piazolo *et al.*, 2008; Wheeler *et al.*, 2009; Montagnat *et al.*, 2011). Systematic characterization of internal grain distortions and their relationship to CPO development will be very important in recognizing deformation regimes and histories in natural samples.

Another reason why EBSD could become very important in ice is that fabric analyzer systems that provide a fast way of mapping *c*-axis distributions are uncommon and expensive to purchase – EBSD is now very readily available and it is easier and cheaper to adapt an existing EBSD setup than to acquire a fabric analyzer system.

Commercial cryostages and their transfer systems limit sample size. Up to now any work on natural glacial samples (Obbard *et al.*, 2006) has required the sample to be cut up into many subsamples to be analyzed separately. The process is time-consuming and there is a risk of losing spatial and orientation reference between the different subsamples. Maps shown in Figures 4(C), 6(E) and 10(A) and (B) are from samples at the absolute upper end of sample sizes that could be exchanged through a conventional cryotransfer system. EBSD maps of areas of this size have not been published before; the effectiveness of the cryomicrotome or grinding methods in generating a large flat surface and the pressure cycle sublimation process in ensuring all of that surface yields good EBSD data are critical in getting data on this scale. Figure 12 shows a data set from a large synthetic columnar ice sample. This sample is much too large to analyze using a conventional cryotransfer system. The sample was too large to prepare in the cryomicrotome and was ground with grit papers down to 1 μm. The sample has dimensions 100 mm by 30 mm by 5 mm thick and was kept stable in the SEM for more than 5 h. Nitrogen gas pressure was reduced to 10 Pa to stop the sample getting too warm; at this pressure, the steady state stage temperature was -80°C. Pressure cycle sublimation (warming to -60°C) was effective even though the sample surface had many scratches from grinding. Lowering the EBSD camera (by 10 mm using the mechanism in Fig. 5A) to enable a long working distance was critical to mapping 30 mm length in the Y direction. Only 70 mm length could be analyzed in the X direction because movement was limited by the length of the Cu braid (Fig. 5C) used for conductive cooling.

The data from the columnar ice illustrate the value of EBSD data over optical data. The horizontal alignment of *c*-axes (Fig. 12C) is well known from optical analysis of columnar ice (Timco & Weeks, 2010; Gough *et al.*, 2012). The fact that there is an equal preference for vertical alignment of the *m* and *a* axes (Fig. 12C) cannot be discerned by optical work.

With the methods we have outlined, analysis of large samples is relatively easy. The sample in Figure 12 is of a similar size to samples that would give statistically representative data in natural glacial ice.

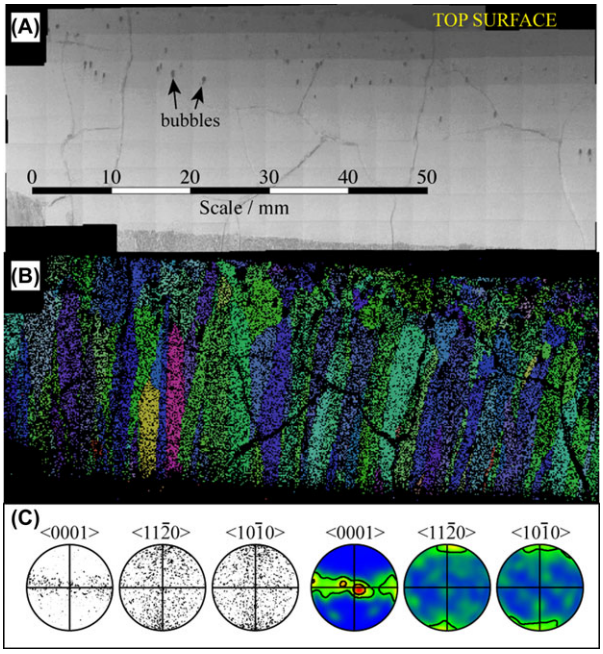

Fig. 12. Large area EBSD map (150 μm step) for a synthetic columnar ice sample cut in a vertical plane. Top surface is the air water interface. (A) Montage of VPSE images showing bubbles in the top 15 mm – the bubbles are more circular near the top and vertically elongated further down. Cracks formed in cooling the sample too rapidly. (B) EBSD IPF Y (see Fig. 4B for legend) map of area shown in A. Dominance of green and blue colours reflects *c*-axes that lie in a horizontal plane. Component individual beam scans (156 of these: linked by stage movement) can be seen in A. (C) Stereonets to show *c*, *a* and *m* directions as point plots and contoured plots. The *c*-axes lie preferentially in a horizontal plane. Contoured plots indicate that both *a* and *m* directions are preferentially vertical – corresponding to blue (*m* vertical) and green (*a* vertical) grains in B.

Ongoing challenges

The methods we have outlined are applicable to low porosity pure water ice (including D_20 ice). There are other samples that we wish to work on that present ongoing challenges.

Porous ice, particularly ice with very high porosity (e.g. snow), needs very careful treatment. The ironing method will not work as the pores will fill with vapour transported ice. The efficacy of the pressure cycle sublimation method will depend upon the distribution of porosity.

We have some success looking at water ice plus hard phases (section 2.2) but there is still significant scope for technique development.

Other ices (CO_2, CH_4, clathrates, etc.) are important in planetary studies (McCarthy *et al.*, 2007; Lenferink *et al.*, 2013), in geosciences (Hester & Brewer, 2009) and in chemical engineering (Sum *et al.*, 2009). We have not yet attempted EBSD on such samples. These will present a variety of challenges (Stern *et al.*, 2004; Donius *et al.*, 2014), including preparation of multiphase surfaces and accommodating differences in sublimation rates between phases.

Our analysis of ice phase transformations is based, so far, on the ice 1h microstructure following transformation from another phase (e.g. ice II). Much better information would be possible if we could collect EBSD data from the ice polymorphs. It is possible to retain high pressure ice polymorphs at low pressure by keeping the temperature very low, where the kinetics of transformation are very slow; indeed, it is possible to retain ice II in an SEM chamber (Stern *et al.*, 1997; Kubo *et al.*, 2006). Our current setup has two limitations – the steady state temperature of imaging ($\sim -100^{\circ}C$) is too high and the processes by which we clean sample surfaces (ironing, pressure cycling) will promote transformation to ice 1h.

Conclusions

- EBSD on low porosity water ice in the Otago laboratory is now routine with a success rate greater than 90%. The methods we present are translatable, with some investment, to any VPSEM with EBSD and a cold stage.
- Sample preparation needs to account for thermal sensitivity of the sample. We present some data on the thermal effects of necessary preparation steps that can be used as guidelines during sample preparation.
- The approaches presented here enable EBSD on fine-grained ice samples.
- The approaches presented here enable EBSD of large surface areas, important in the analysis of natural ice samples.
- Avenues for future work include porous ice, ice mixed with hard particles, multicomponent ices, and ice polymorphs.

Acknowledgements

Intern students Kathy Cresswell-Moorcock, Alex Wilson and Imogen Browne helped develop systems for making synthetic ice samples. Brent Pooley in Geology, Jim Woods and Leo van Rens of the EMTECH mechanical workshop and Trevor Douglas of Trevor Douglas plastics manufactured custom equipment. Peter Fleury designed and built electrical and electronic systems. Kai Chun Li prepared the zirconia plate for ironing. Staff at Para Rubber helped in selecting sealing systems for the glove box. Jason Grieve helped out with sample handling. Allan Mitchell, Liz Girvan, Gillian Grayston and Sharon Lequeux, all of Otago Centre for Electron Microscopy, helped significantly in acquiring ancillary equipment we needed and ensuring we had all facilities available during ice EBSD campaigns. Mandy Fisher of the histology laboratory advised on microtome blades. Pat Langhorne provided cold room facilities in Physics. Jan Leunissen (Aurion), Mike Strauss (Harvard), Mihnea Bostina (Otago Center for Electron Microscopy) and Jevon Longdell provided useful insights into ice/water behaviour and heat transfer. Chris Gerbi and an anonymous reviewer provided useful suggestions that improved clarity of the manuscript. This research was supported by NERC grant NE/G01034×1/1, Marsden Fund grant UOO1116, NASA grant NNX13AK98G and a University of Otago research grant. L. Becroft (MSc), M. Seidemann (PhD) and M. Vaughan (PhD) are funded by University of Otago scholarships.

References

Alley, R. B. & Woods, G. A. (1996). Impurity influence on normal grain growth in the GISP2 ice core, Greenland. *J. Glaciol.* **42**(141), 255–260.

Alley, R. B., Perepezko, J. H. & Bentley, C. R. (1986). Grain-growth in polar ice .2. Application. *J. Glaciol.* **32**(112), 425–433.

Alley, R. B., Bentley, C. R. & Perepezko, J. H. (1987). Grain-growth in unstrained glacial ice. *J. Phys.-Paris* **48**(C-1), 659–660.

Andreas, E. L. (2007). New estimates for the sublimation rate for ice on the Moon. *Icarus* **186**(1), 24–30.

Austin, N. J. & Evans, B. (2007). Paleowattmeters: a scaling relation for dynamically recrystallized grain size. *Geology* **35**(4), 343–346.

Azuma, N., Miyakoshi, T., Yokoyama, S. & Takata, M. (2012). Impeding effect of air bubbles on normal grain growth of ice. *J. Struct. Geol.* **42**, 184–193.

Bachmann, F., Hielscher, R. & Schaeben, H. (2010). Texture analysis with MTEX – free and open source software toolbox. *Texture and Anisotropy of Polycrystals III* (eds. by H. Klein & R.A. Schwarzer), vol. **160**, pp. 63–68. Trans Tech Publications Ltd, Switzerland.

Barnes, P. R. F., Mulvaney, R., Wolff, E. W. & Robinson, K. (2002). A technique for the examination of polar ice using the scanning electron microscope. *J. Microsc.-Oxford* **205**, 118–124.

Barr, A. C. & McKinnon, W. B. (2007). Convection in ice I shells and mantles with self-consistent grain size. *J. Geophys. Res.-Planet* **112**(E2).

Bentley, C. R. & Koci, B. R. (2007). Drilling to the beds of the Greenland and Antarctic ice sheets: a review. *Ann. Glaciol.* **47**, 1–9.

Bestmann, M. & Prior, D. J. (2003). Intragranular dynamic recrystallization in naturally deformed calcite marble: diffusion accommodated grain boundary sliding as a result of subgrain rotation recrystallization. *J. Struct. Geol.* **25**(10), 1597–1613.

Bielska, K., Havey, D. K., Scace, G. E., Lisak, D., Harvey, A. H. & Hodges, J. T. (2013). High-accuracy measurements of the vapor pressure of ice referenced to the triple point. *Geophys. Res. Lett.* **40**(23), 6303–6307.

Binder, T., Garbe, C. S., Wagenbach, D., Freitag, J. & Kipfstuhl, S. (2013). Extraction and parametrization of grain boundary networks in glacier ice, using a dedicated method of automatic image analysis. *J. Microsc.* **250**(2), 130–141.

Budd, W. F. & Jacka, T. H. (1989). A review of ice rheology for ice-sheet modeling. *Cold Reg. Sci. Technol.* **16**(2), 107–144.

Cross, J. D. (1969). Scanning electron microscopy of evaporating ice. *Science* **164**(3876), 174–175.

Cuffey, K. M. & Kavanaugh, J. L. (2011). How nonlinear is the creep deformation of polar ice? A new field assessment. *Geology* **39**(11), 1027–1030.

Cuffey, K. M. & Paterson, W. S. B. (2010). *The Physics of Glaciers*. Elsevier, Amsterdam. p. 693.

De Bresser, J. H. P., Ter Heege, J. H. & Spiers, C. J. (2001). Grain size reduction by dynamic recrystallization: can it result in major theological weakening? *Int. J. Earth Sci.* **90**(1), 28–45.

Donius, A. E., Obbard, R. W., Burger, J. N., Hunger, P. M., Baker, I., Doherty, R. D. & Wegst, U. G. K. (2014). Cryogenic EBSD reveals structure of directionally solidified ice-polymer composite. *Mater. Charact.* **93**, 184–190.

Durham, W. B., Kirby, S. H., Heard, H. C. & Stern, L. A. (1987). Inelastic properties of several high-pressure crystalline phases of h2o – ice-II, ice-III and ice-V. *J. Phys.-Paris* **48**(C-1), 221–226.

Durham, W. B., Kirby, S. H. & Stern, L. A. (1992). Effects of dispersed particulates on the rheology of water ice at planetary conditions. *J. Geophys. Res.-Planet* **97**(E12), 20883–20897.

Durham, W. B., Prieto-Ballesteros, O., Goldsby, D. L. & Kargel, J. S. (2010). Rheological and thermal properties of icy materials. *Space Sci. Rev.* **153**(1–4), 273–298.

Duval, P. & Castelnau, O. (1995). Dynamic recrystallization of ice in polar ice sheets. *J. Phys. IV* **5**(C3), 197–205.

Duval, P., Ashby, M. F. & Anderman, I. (1983). Rate-controlling processes in the creep of polycrystalline ice. *J. Phys. Chem.* **87**(21), 4066–4074.

Duval, P., Montagnat, M., Grennerat, F., Weiss, J., Meyssonnier, J. & Philip, A. (2010). Creep and plasticity of glacier ice: a material science perspective. *J. Glaciol.* **56**(200), 1059–1068.

Erbe, E. F., Rango, A., Foster, J., Josberger, E. G., Pooley, C. & Wergin, W. P. (2003). Collecting, shipping, storing, and imaging snow crystals and ice grains with low-temperature scanning electron mircoscopy. *Microsc. Res. Techniq.* **62**(1), 19–32.

Evans, B., Renner, J. & Hirth, G. (2001). A few remarks on the kinetics of static grain growth in rocks. *Int. J. Earth Sci.* **90**(1), 88–103.

Faria, S. H., Weikusat, I. & Azuma, N. (2014a). The microstructure of polar ice. Part I: highlights from ice core research. *J. Struct. Geol.* **61**, 2–20.

Faria, S. H., Weikusat, I. & Azuma, N. (2014b). The microstructure of polar ice. Part II: state of the art. *J. Struct. Geol.* **61**, 21–49.

Field, D. P., Bradford, L. T., Nowell, M. M. & Lillo, T. M. (2007). The role of annealing twins during recrystallization of Cu. *Acta Mater.* **55**(12), 4233–4241.

Fynn, G. W. & Powell, W. J. A. (1979). *The Cutting and Polishing of Electro-Optic Materials*. Adams Hilger, London, p. 216.

Gagliardini, O., Zwinger, T. & Gillet-Chaulet, F. *et al.* (2013). Capabilities and performance of Elmer/ice, a new-generation ice sheet model. *Geosci. Model Dev.* **6**(4), 1299–1318.

Godert, G. & Hutter, K. (1998). Induced anisotropy in large ice shields: theory and its homogenization. *Continuum Mech. Therm.* **10**(5), 293–318.

Golding, N., Schulson, E. M. & Renshaw, C. E. (2012). Shear localization in ice: mechanical response and microstructural evolution of P-faulting. *Acta Mater.* **60**(8), 3616–3631.

Goldsby, D. L. (2006). Superplastic flow of ice relevant to glacier and ice-sheet mechanics. *Glacier Science and Environmental Change* (eds. by P.G. Knight), pp. 308–314. Blackwell, Oxford.

Goldsby, D. L. & Kohlstedt, D. L. (1997). Grain boundary sliding in fine-grained Ice I. *Scripta Mater.* **37**(9), 1399–1406.

Gough, A. J., Mahoney, A. R., Langhorne, P. J., Williams, M. J. M. & Haskell, T. G. (2012). Sea ice salinity and structure: a winter time series of salinity and its distribution. *J. Geophys. Res.-Oceans* **117**.

Harland, S. R., Kendall, J. M., Stuart, G. W., Lloyd, G. E., Baird, A. F., Smith, A. M., Pritchard, H. D. & Brisbourne, A. M. (2013). Deformation in Rutford Ice Stream, West Antarctica: measuring shear-wave anisotropy from icequakes. *Ann. Glaciol.* **54**(64), 105–114.

Hester, K. C. & Brewer, P. G. (2009). Clathrate hydrates in nature. *Annu. Rev. Mar. Sci.* **1**, 303–327.

Humphreys, F. J. (1999). Quantitative metallography by electron backscattered diffraction. *J. Microsc.-Oxford* **195**, 170–185.

Humphreys, F. J. & Hatherley. (1996). *Recrystallization and Related Annealing Phenomena*. Elsevier Science, Kidlington, p. 498.

Iliescu, D., Baker, I. & Chang, H. (2004). Determining the orientations of ice crystals using electron backscatter patterns. *Microsc. Res. Techniq.* **63**(4), 183–187.

Jacka, T. H. & Jun, L. (1994). The steady-state crystal size of deforming ice. *Ann. Glaciol.* **20**, 13–18.

Joughin, I., Bindschadler, R. A. & King, M. A. *et al.* (2005). Continued deceleration of Whillans Ice Stream, West Antarctica. *Geophys. Res. Lett.* **32**(22).

Kubo, T., Durham, W. B., Stern, L. A. & Kirby, S. H. (2006). Grain size-sensitive creep in ice II. *Science* **311**(5765), 1267–1269.

Law, R. D., Mainprice, D., Casey, M., Lloyd, G. E., Knipe, R. J., Cook, B. & Thigpen, J. R. (2010). Moine thrust zone mylonites at the stack of glencoul. *I – Microstructures, Strain and Influence of Recrystallization on Quartz Crystal Fabric Development* **335**, 543–577.

Lenferink, H. J., Durham, W. B., Stern, L. A. & Pathare, A. V. (2013). Weakening of ice by magnesium perchlorate hydrate. *Icarus* **225**(2), 940–948.

Lloyd, G. E. (1987). Atomic-number and crystallographic contrast images with the SEM – a review of backscattered electron techniques. *Mineral. Mag.* **51**(359), 3–19.

Lloyd, G. E. (2004). Microstructural evolution in a mylonitic quartz simple shear zone: the significant roles of dauphine twinning and misorientation. *Flow Processes in Faults and Shear Zones* (eds. by G.I. Alsop, R.E. Holdsworth, K.J.W. McCaffrey & M. Hand), Geological Society Special Publication, Vol. **224**, pp. 39–61, London.

Lloyd, G. E., Farmer, A. B. & Mainprice, D. (1997). Misorientation analysis and the formation and orientation of subgrain and grain boundaries. *Tectonophysics* **279**(1–4), 55–78.

Macayeal, D. R. (1989). Large-scale ice flow over a viscous basal sediment – theory and application to ice stream-B, Antarctica. *J. Geophys. Res.-Solid* **94**(B4), 4071–4087.

McCarthy, C., Cooper, R. F., Kirby, S. H., Rieck, K. D. & Stern, L. A. (2007). Solidification and microstructures of binary ice-I/hydrate eutectic aggregates. *Am. Mineral.* **92**(10), 1550–1560.

McDaniel, S., Bennett, K., Durham, W. B. & Waddington, E. D. (2006). In situ deformation apparatus for time-of-flight neutron diffraction: texture development of polycrystalline ice I-h. *Rev. Sci. Instrum.* **77**(9).

McDonald, K. & Muller-Reichert, T. (2008). Introduction: themed issue on high-pressure freezing. *J. Microsc.-Oxford* **230**(2), 252.

Miyamoto, A., Weikusat, I. & Hondoh, T. (2011). Complete determination of ice crystal orientation using Laue X-ray diffraction method. *J. Glaciol.* **57**(201), 103–110.

Montagnat, M., Duval, P., Bastie, P., Hamelin, B. & Lipenkov, V. Y. (2003). Lattice distortion in ice crystals from the Vostok core (Antarctica) revealed by hard X-ray diffraction: implication in the deformation of ice at low stresses. *Earth Planet. Sci. Lett.* **214**(1–2), 369–378.

Montagnat, M., Blackford, J. R., Piazolo, S., Arnaud, L. & Lebensohn, R. A. (2011). Measurements and full-field predictions of deformation heterogeneities in ice. *Earth Planet. Sci. Lett.* **305**(1–2), 153–160.

Montagnat, M., Castelnau, O. & Bons, P. D. *et al.* (2014). Multiscale modeling of ice deformation behavior. *J. Struct. Geol.* **61**, 78–108.

Murray, B. J., Knopf, D. A. & Bertram, A. K. (2005). The formation of cubic ice under conditions relevant to Earth's atmosphere. *Nature* **434**(7030), 202–205.

Obbard, R., Baker, I. & Sieg, K. (2006). Using electron backscatter diffraction patterns to examine recrystallization in polar ice sheets. *J. Glaciol.* **52**(179), 546–557.

Obbard, R. W., Baker, I. & Prior, D. J. (2011). A scanning electron microscope technique for identifying the mineralogy of dust in ice cores. *J. Glaciol.* **57**(203), 511–514.

Peruzzo, L., Fenzi, F. & Vigato, P. A. (2011). Electron backscatter diffraction (EBSD): a new technique for the identification of pigments and raw materials in historic glasses and ceramics. *Archaeometry* **53**, 178–193.

Piazolo, S., Montagnat, M. & Blackford, J. R. (2008). Sub-structure characterization of experimentally and naturally deformed ice using cryo-EBSD. *J. Microsc.-Oxford* **230**(3), 509–519.

Piazolo, S., Wilson, C. J. L., Luzin, V., Brouzet, C. & Peternell, M. (2013). Dynamics of ice mass deformation: linking processes to rheology, texture, and microstructure. *Geochem. Geophys. Geosyst.* **14**(10), 4185–4194.

Poirier, J. P. (1982). Rheology of Ices – a key to the tectonics of the Ice Moons of Jupiter and Saturn. *Nature* **299**(5885), 683–688.

Prior, D. J., Boyle, A. P. & Brenker, F. *et al.* (1999). The application of electron backscatter diffraction and orientation contrast imaging in the SEM to textural problems in rocks. *Am. Mineral.* **84**(11–12), 1741–1759.

Prior, D. J., Wheeler, J., Peruzzo, L., Spiess, R. & Storey, C. (2002). Some garnet micro structures: an illustration of the potential of orientation maps and misorientation analysis in microstructural studies. *J. Struct. Geol.* **24**(6–7), 999–1011.

Prior, D. J., Mariani, E. & Wheeler, J. (2009). EBSD in the earth sciences: applications, common practice and challenges. *Electron Backscatter Diffraction in Materials Science* (eds. by A.J. Schwartz, M. Kumar, B.L. Adams & D.P. Field), pp. 345–360. Springer US, New York, NY, USA.

Prior, D. J., Diebold, S., Obbard, R., Daghlian, C., Goldsby, D. L., Durham, W. B. & Baker, I. (2012). Insight into the phase transformations between ice Ih and ice II from electron backscatter diffraction data. *Scripta Mater.* **66**(2), 69–72.

Riche, F., Montagnat, M. & Schneebeli, M. (2013). Evolution of crystal orientation in snow during temperature gradient metamorphism. *J. Glaciol.* **59**(213), 47–55.

Riikonen, M., Sillanpaa, M., Virta, L., Sullivan, D., Moilanen, J. & Luukkonen, I. (2000). Halo observations provide evidence of airborne cubic ice in the Earth's atmosphere. *Appl. Optics* **39**(33), 6080–6085.

Roessiger, J., Bons, P. D. & Faria, S. H. (2014). Influence of bubbles on grain growth in ice. *J. Struct. Geol.* **61**, 123–132.

Rohrer, G. S. (2011). Grain boundary energy anisotropy: a review. *J. Mater. Sci.* **46**(18), 5881–5895.

Rohrer, G. S., Saylor, D. M., El Dasher, B., Adams, B. L., Rollett, A. D. & Wynblatt, P. (2004). The distribution of internal interfaces in polycrystals. *Z. Metallkd.* **95**(4), 197–214.

Rozmanov, D. & Kusalik, P. G. (2012). Anisotropy in the crystal growth of hexagonal ice, I-h. *J. Chem. Phys.* **137**(9).

Salzmann, C. G., Radaelli, P. G., Slater, B. & Finney, J. L. (2011). The polymorphism of ice: five unresolved questions. *Phys. Chem. Chem. Phys.* **13**(41), 18468–18480.

Samyn, D., Azuma, N., Matsuda, I. & Osabe, Y. (2014). Novel shearing apparatuses in confined flow for investigating recrystallization and fabric evolution processes in mono- and polycrystalline ice. *J. Glaciol.* **60**(219), 171–182.

Sander, B. (1970). *An Introduction to the Study of Fabrics of Geological Bodies (English Translation)*. Pergamon, Oxford, p. 641.

Saylor, D. M. & Rohrer, G. S. (1999). Measuring the influence of grain-boundary misorientation on thermal groove geometry in ceramic polycrystals. *J. Am. Ceram. Soc.* **82**(6), 1529–1536.

Schwartz, A. J., Kumar, M., Adams, B. L. & Field, D. P. (2009). *Electron Backscatter Diffraction in Materials Sciences*. Springer US, New York, NY, USA.

Spaulding, N. E., Meese, D. A. & Baker, I. (2011). Advanced microstructural characterization of four East Antarctic firn/ice cores. *J. Glaciol.* **57**(205), 796–810.

Stern, L. A., Durham, W. B. & Kirby, S. H. (1997). Grain-size-induced weakening of H2O ices I and II and associated anisotropic recrystallization. *J. Geophys Res.-Sol. Ea.* **102**(B3), 5313–5325.

Stern, L. A., Kirby, S. H., Circone, S. & Durham, W. B. (2004). Scanning electron microscopy investigations of laboratory-grown gas clathrate hydrates formed from melting ice, and comparison to natural hydrates. *Am. Mineral.* **89**(8–9), 1162–1175.

Stipp, M., Tullis, J., Scherwath, M. & Behrmann, J. H. (2010). A new perspective on paleopiezometry: dynamically recrystallized grain size distributions indicate mechanism changes. *Geology* **38**(8), 759–762.

Sum, A. K., Koh, C. A. & Sloan, E. D. (2009). Clathrate hydrates: from laboratory science to engineering practice. *Ind. Eng. Chem. Res.* **48**(16), 7457–7465.

Timco, G. W. & Weeks, W. F. (2010). A review of the engineering properties of sea ice. *Cold Reg. Sci. Technol.* **60**(2), 107–129.

Twiss, R. J. (1977). Theory and applicability of a recrystallized grain-size paleopiezometer. *Pure Appl. Geophys.* **115**(1–2), 227–244.

Urai, J. L. & Jessell, M. (2001). Recrystallization and grain growth in minerals: recent developments. In *Proceedings of the First Joint International Conference on Recrystallization and Grain Growth* (eds. by G. Gottstein & D. Molodov). Springer Verlag, Berlin, pp. 87–95.

Wagner, W. & Pruss, A. (2002). The IAPWS formulation 1995 for the thermodynamic properties of ordinary water substance for general and scientific use. *J. Phys. Chem. Ref. Data* **31**(2), 387–535.

Wagner, W., Riethmann, T., Feistel, R. & Harvey, A. H. (2011). New equations for the sublimation pressure and melting pressure of H2O ice Ih. *J. Phys. Chem. Ref. Data* **40**(4).

Weikusat, I., De Winter, D. A. M., Pennock, G. M., Hayles, M., Schneijdenberg, C. T. W. M. & Drury, M. R. (2011). Cryogenic EBSD on ice: preserving a stable surface in a low pressure SEM. *J. Microsc.-Oxford* **242**, 295–310.

Weikusat, I., Miyamoto, A., Faria, S. H., Kipfstuhl, S., Azuma, N. & Hondoh, T. (2011). Subgrain boundaries in Antarctic ice quantified by X-ray Laue diffraction. *J. Glaciol.* **57**(201), 111–120.

Whalley, E. (1981). Scheiners halo – evidence for ice Ic in the atmosphere. *Science* **211**(4480), 389–390.

Wheeler, J., Prior, D. J., Jiang, Z., Spiess, R. & Trimby, P. W. (2001). The petrological significance of misorientations between grains. *Contrib. Mineral. Petr.* **141**(1), 109–124.

Wheeler, J., Mariani, E., Piazolo, S., Prior, D. J., Trimby, P. & Drury, M. R. (2009). The weighted Burgers vector: a new quantity for constraining dislocation densities and types using electron backscatter diffraction on 2D sections through crystalline materials. *J. Microsc.-Oxford* **233**(3), 482–494.

Wilen, L. A., Diprinzio, C. L., Alley, R. B. & Azuma, N. (2003). Development, principles, and applications of automated ice fabric analyzers. *Microsc. Res. Techniq.* **62**(1), 2–18.

Wilson, C. J. L. & Peternell, M. (2011). Evaluating ice fabrics using fabric analyser techniques in Sorsdal Glacier, East Antarctica. *J. Glaciol.* **57**(205), 881–894.

Wilson, C. J. L. & Russellhead, D. S. (1982). Steady-state preferred orientation of ice deformed in plane-strain at -1-degree-C. *J. Glaciol.* **28**(98), 145–160.

Wilson, C. J. L., Peternell, M., Piazolo, S. & Luzin, V. (2014). Microstructure and fabric development in ice: lessons learned from in situ experiments and implications for understanding rock evolution. *J. Struct. Geol.* **61**, 50–77.